Dust spectrum and polarisation at 850 μ m in the massive IRDC G035.39-00.33

Mika Juvela, V. Guillet, Tie T. Liu, Isabelle Ristorcelli, Veli-Matti Pelkonen, Dana Alina, Leonardo Bronfman, David J. Eden, Kee Tae Kim, Patrick M. Koch, et al.

A&A 620, A26 (2018)
https://doi.org/10.1051/0004-6361/201833245

Astronomy & Astrophysics

Dust spectrum and polarisation at 850 μm in the massive IRDC G035.39-00.33

Mika Juvela[1], Vincent Guillet[2,3], Tie Liu[4,5], Isabelle Ristorcelli[6,7], Veli-Matti Pelkonen[1], Dana Alina[8], Leonardo Bronfman[9], David J. Eden[10], Kee Tae Kim[4], Patrick M. Koch[11], Woojin Kwon[4,12], Chang Won Lee[4,12], Johanna Malinen[13], Elisabetta Micelotta[1], Julien Montillaud[14], Mark G. Rawlings[5], Patricio Sanhueza[15], Archana Soam[4,16], Alessio Traficante[17], Nathalie Ysard[2], and Chuan-Peng Zhang[18,19]

[1] Department of Physics, University of Helsinki, PO Box 64, 00014 Helsinki, Finland
e-mail: mika.juvela@helsinki.fi
[2] Institut d'Astrophysique Spatiale, CNRS, Université Paris-Sud, Université Paris-Saclay, Bât. 121, 91405 Orsay Cedex, France
[3] Laboratoire Univers et Particules de Montpellier, Université de Montpellier, CNRS/IN2P3, CC 72, Place Eugène Bataillon, 34095 Montpellier Cedex 5, France
[4] Korea Astronomy and Space Science Institute, 776 Daedeokdaero, Yuseong-gu, Daejeon 34055, Republic of Korea
[5] East Asian Observatory, 660 N. A'ohōkū Place, Hilo, HI 96720-2700, USA
[6] Université de Toulouse, UPS-OMP, IRAP, 31028 Toulouse Cedex 4, France
[7] CNRS, IRAP, 9 Av. colonel Roche, BP 44346, 31028 Toulouse Cedex 4, France
[8] Department of Physics, School of Science and Technology, Nazarbayev University, Astana 010000, Kazakhstan
[9] Departamento de Astronomía, Universidad de Chile, Casilla 36-D, Santiago, Chile
[10] Astrophysics Research Institute, Liverpool John Moores University, Ic2, Liverpool Science Park, 146 Brownlow Hill, Liverpool, L3 5RF, UK
[11] Academia Sinica, Institute of Astronomy and Astrophysics, Taipei, Taiwan
[12] Korea University of Science and Technology, 217 Gajang-ro, Yuseong-gu, Daejeon 34113, Republic of Korea
[13] Institute of Physics I, University of Cologne, Cologne, Germany
[14] Institut UTINAM, CNRS UMR 6213, OSU THETA, Université de Franche-Comté, 41bis avenue de l'Observatoire, 25000 Besançon, France
[15] National Astronomical Observatory of Japan, National Institutes of Natural Sciences, 2-21-1 Osawa, Mitaka, Tokyo 181-8588, Japan
[16] SOFIA Science Center, Universities Space Research Association, NASA Ames Research Center, Moffett Field, CA 94035, USA
[17] IAPS – INAF, via Fosso del Cavaliere, 100, 00133 Roma, Italy
[18] National Astronomical Observatories, Chinese Academy of Sciences, 100012 Beijing, PR China
[19] Max-Planck-Institut für Astronomie, Königstuhl 17, 69117 Heidelberg, Germany

Received 17 April 2018 / Accepted 3 September 2018

ABSTRACT

Context. The sub-millimetre polarisation of dust emission from star-forming clouds carries information on grain properties and on the effects that magnetic fields have on cloud evolution.
Aims. Using observations of a dense filamentary cloud G035.39-00.33, we aim to characterise the dust emission properties and the variations of the polarisation fraction.
Methods. JCMT SCUBA-2/POL-2 observations at 850 μm were combined with *Planck* 850 μm (353 GHz) data to map polarisation fraction at small and large scales. With previous total intensity SCUBA-2 observations (450 and 850 μm) and *Herschel* data, the column densities were determined via modified black-body fits and via radiative transfer modelling. Models were constructed to examine how the observed polarisation angles and fractions depend on potential magnetic field geometries and grain alignment processes.
Results. POL-2 data show clear changes in the magnetic field orientation. These are not in contradiction with the uniform orientation and almost constant polarisation fraction seen by *Planck*, because of the difference in the beam sizes and the POL-2 data being affected by spatial filtering. The filament has a peak column density of $N(\mathrm{H_2}) \sim 7 \times 10^{22}$ cm^{-2}, a minimum dust temperature of $T \sim 12$ K, and a mass of ~4300 $M_\odot$ for the area $N(\mathrm{H_2}) > 5 \times 10^{21}$ cm^{-2}. The estimated average value of the dust opacity spectral index is $\beta \sim 1.9$. The ratio of sub-millimetre and J-band optical depths is τ (250 μm)/τ (J) $\sim 2.5 \times 10^{-3}$, more than four times the typical values for diffuse medium. The polarisation fraction decreases as a function of column density to $p \sim 1\%$ in the central filament. Because of noise, the observed decrease of $p(N)$ is significant only at $N(\mathrm{H_2}) > 2 \times 10^{22}$ cm^{-2}. The observations suggest that the grain alignment is not constant. Although the data can be explained with a complete loss of alignment at densities above $\sim 10^4$ cm^{-3} or using the predictions of radiative torques alignment, the uncertainty of the field geometry and the spatial filtering of the SCUBA-2 data prevent strong conclusions.
Conclusions. The G035.39-00.33 filament shows strong signs of dust evolution and the low polarisation fraction is suggestive of a loss of polarised emission from its densest parts.

Key words. ISM: clouds – infrared: ISM – submillimeter: ISM – dust, extinction – stars: formation – stars: protostars

1. Introduction

Filamentary structures play an important role in star formation, from cloud formation to the birth of clumps and gravitationally bound pre-stellar cores. Filaments range from infrared dark clouds (IRDCs), with lengths up to tens of parsecs (Elmegreen & Elmegreen 1979; Egan et al. 1998; Goodman et al. 2014; Wang et al. 2015), to the parsec-scale star-forming filaments of nearby molecular clouds (Bally et al. 1987; André et al. 2010; Men'shchikov et al. 2010; Arzoumanian et al. 2011; Hill et al. 2011; Schneider et al. 2012; Hennemann et al. 2012; Juvela et al. 2012; André et al. 2014; Rivera-Ingraham et al. 2016), and further down in linear scale to thin fibres as sub-structures of dense filaments (Hacar et al. 2013, 2018; Fernández-López et al. 2014) and to low-column-density striations (Palmeirim et al. 2013; Cox et al. 2016; Heyer et al. 2016; Miettinen 2018).

Most likely all filaments do not have a common origin. The formation of an individual structure can be the result of random turbulent motions (Ballesteros-Paredes et al. 1999; Padoan et al. 2001; Klassen et al. 2017; Li et al. 2018), cloud–cloud collisions, triggering by external forces (Hennebelle et al. 2008; Federrath et al. 2010; Wu et al. 2017; Anathpindika et al. 2018; Liu et al. 2018a,b), or a combination of several factors. The effects on star formation are closely connected to the role that magnetic fields have in the formation of filaments and later in the fragmentation and the support of gravitationally bound structures.

Our knowledge of the magnetic fields in filamentary clouds is largely based on polarisation, the optical and near-infrared (NIR) polarisation observations of the light from background stars and the polarised dust emission at far-infrared (FIR), sub-millimetre, and radio wavelengths. These methods are partly complementary, extinction studies probing diffuse regions and clouds up to visual extinctions of $A_V \sim 20^m$ (Goodman et al. 1995; Neha et al. 2018; Kandori et al. 2018), while ground-based emission studies cover the range of $A_V \sim 1-100^m$ (Ward-Thompson et al. 2000; Pattle et al. 2017; Kwon et al. 2018; Liu et al. 2018b). The magnetic field appears to be mainly (but not perfectly) orthogonal to the main axis of some nearby filamentary clouds such as the Musca (Pereyra & Magalhães 2004; Cox et al. 2016), Taurus (Heyer et al. 1987; Goodman et al. 1990; Planck Collaboration Int. XXXV 2016), Pipe (Alves et al. 2008), and Lupus I (Matthews et al. 2014) molecular clouds. This also means that the fainter striations, which tend to be perpendicular to high-column-density filaments, are aligned with the magnetic field orientation. It has been suggested that the striations represent accretion onto the potentially star-forming filaments, the inflow thus being funnelled by the magnetic fields (Palmeirim et al. 2013). Studies with *Planck* data have found that the column density structures tend to be aligned with the magnetic field in diffuse clouds while in the molecular clouds and at higher densities the orthogonal configuration is more typical (Planck Collaboration Int. XXXII 2016; Planck Collaboration Int. XXXV 2016; Malinen et al. 2016; Alina et al. 2018). The orthogonal configuration was typical also for the dense clouds that were observed with ground-based telescopes in Koch et al. (2014). A similar trend in the relative orientations at low and high column densities is reported for numerical simulations (Soler et al. 2013; Klassen et al. 2017; Li et al. 2018). The orthogonal geometry seems dominant even in the most massive filaments and in regions of active star formation. However, the situation can be complicated by the effects of local gravitational collapse, stellar feedback, and the typically higher levels of background and foreground emission (Santos et al. 2016; Pattle et al. 2017; Hoq et al. 2017).

The polarisation fraction p appears to be negatively correlated with the column density (Vrba et al. 1976; Gerakines et al. 1995; Ward-Thompson et al. 2000; Alves et al. 2014; Planck Collaboration Int. XIX 2015), although sometimes the relation is difficult to separate from the noise-induced bias that affects observations at low signal-to-noise ratios (S/N). The column-density dependence of p has also been studied statistically in connection with clumps and filaments (Planck Collaboration Int. XXXIII 2016; Ristorcelli et al., in prep.). This raises the question whether the decrease is caused by a specific magnetic field geometry (such as small-scale line tangling or changes in the large-scale magnetic field orientation) or by factors related to the grain alignment. The radiative torques (RAT) are a strong candidate for a mechanism behind the grain alignment (Lazarian et al. 1997; Hoang & Lazarian 2014). Because RAT require radiation to spin up the dust grains, they naturally predicts a loss of polarisation at high A_V. The effect depends on the grain properties and is thus affected by the grain growth that is known to take place in dense environments (Whittet et al. 2001; Stepnik et al. 2003; Ysard et al. 2013; Voshchinnikov et al. 2013). If RAT are the main cause of grain alignment, it is difficult to produce any significant polarised emission from very dense clumps and filaments (Pelkonen et al. 2009). On the other hand, numerical simulations also have shown the significance of geometrical depolarisation, which would still probe the magnetic field configurations at lower column densities (Planck Collaboration Int. XX 2015; Chen et al. 2016a).

We have studied the filamentary IRDC G035.39-00.33, which has a mass of some 17 000 $M_\odot$ (Kainulainen & Tan 2013) and is located at a distance of 2.9 Kpc (Simon et al. 2006). The source corresponds to PGCC G35.49-0.31 in the *Planck* catalogue of Galactic Cold Clumps (Planck Collaboration XXVIII 2016). The field has been targeted by several recent studies in both molecular lines and in continuum (e.g. Zhang et al. 2017; Liu et al. 2018b). Although the single-dish infrared and sub-millimetre images of G035.39-00.33 are dominated by a single ~5 pc long structure, high-resolution line observations have revealed the presence of velocity-coherent, ~0.03 pc wide sub-filaments or fibres (Henshaw et al. 2017). The filament is associated with a number of dense cores that, while being cold ($T \lesssim 16$ K) and IR-quiet, may have potential for future high-mass star formation (Nguyen Luong et al. 2011; Liu et al. 2018b). There are a number of low luminosity (Class 0) protostars but G035.39-00.33 appears to be in an early stage of evolution where the cloud structure is not yet strongly affected by the stellar feedback. This makes G035.39-00.33 a good target for studies of dust polarisation. Liu et al. (2018b) already discussed the magnetic field morphology in G035.39-00.33 based on POL-2 observations made with the *James Clerk Maxwell* Telescope (JCMT) SCUBA-2 instrument. Liu et al. (2018b) estimated that the average plane-of-the-sky (POS) magnetic field strength is ~50 μG and the field might provide significant support for the clumps in the filament against gravitational collapse. The pinched magnetic field morphology in its southern part was suggested to be related to accretion flows along the filament.

In this paper we will use *Planck*, *Herschel*, and JCMT/POL-2 observations to study the structure, dust emission spectrum, and polarisation properties of G035.39-00.33. In particular, we investigate the polarisation fraction variations, its column-density dependence, and the interpretations in terms of magnetic field geometry and grain alignment efficiency. After describing the observations in Sect. 2 and the methods in Sect. 3, the main results are presented in Sect. 4. These include estimates of dust opacity (Sect. 4.3) and polarisation fraction (Sect. 4.6).

Table 1. Observation IDs of the data used.

Observation	Observation ID
G035.39-00.33/SCUBA-2	scuba2_00063_20160413T170550
G035.39-00.33/POL-2	scuba2_00011_20170814T073201
Uranus/SCUBA-2	scuba2_00021_20171109T074149
	scuba2_00027_20171110T094533
	scuba2_00042_20171110T125528
	scuba2_00032_20171120T092415

The radiative transfer models for the total intensity and for the polarised emission are presented in Sect. 5. We discuss the results in Sect. 6 before presenting the conclusions in Sect. 7.

2. Observational data

2.1. JCMT observations

The observations with the JCMT SCUBA-2 instrument (Holland et al. 2013) are described in detail in Liu et al. (2018b). We use the 850 μm (total intensity and polarisation) and 450 μm (total intensity) data. First total intensity observations were carried out in April 2016 as part of the SCOPE programme (Liu et al. 2018a).

The POL-2 polarisation measurements were made between June and November 2017 using the POL-2 DAISY mapping mode (project code: M17BP050; PI: Tie Liu). The field was covered by two mappings, each covering a circular region with a diameter of 12′. The maps were created with the pol2map routine of the Starlink SMURF package. The final co-added maps have an rms noise of ∼1.5 mJy beam^{-1}. The map making employed a filtering scale of $\theta_F = 200''$, which removes extended emission but results in good fidelity to structures smaller than θ_F (Mairs et al. 2015). For further details of the observations, see Liu et al. (2018b).

We assume for SCUBA-2 a 10% uncertainty, which covers the calibration uncertainty as an absolute error relative to the other data sets. The contamination of the 850 μm band by CO J = 3–2 could be a source of systematic positive error. Although the CO contribution in 850 μm measurements can sometimes reach tens of percent (Drabek et al. 2012), it is usually below 10% (e.g. Moore et al. 2015; Mairs et al. 2016; Juvela et al. 2018). Parts of the G035.39-00.33 field have been mapped with the JCMT/HARP instrument (observation ID JCMT_1307713342_798901). The ^{12}CO(3–2) line area (in main beam temperature T_{MB}) towards the northern clump reaches 66 K km s^{-1}. This corresponds to a 8.3 mJy sr^{-1} (46 mJy beam^{-1}) contamination in the 850 μm continuum value, which is some 8% of the measured surface brightness. However, this does not take into account that observations filter out all large-scale emission. The average ^{12}CO signal at 2′ distance of this position is still some 7 mJy sr^{-1}. When the large-scale emission is filtered out, the residual effect on the 850 μm surface brightness should be ∼2% or less and small compared to the assumed total uncertainty of 10%. Therefore, we do not apply any corrections to the 850 μm values.

The FWHM of the SCUBA-2 main beam is ∼14″ at 850 μm and ∼8″ at 450 μm. Because the beam patterns include a wider secondary component (Dempsey et al. 2013), we used Uranus measurements (see Table 1) to derive spherically symmetric beam patterns. The planet size, which was ∼3.7″ at the time of the observations, has little effect on the estimated beams and is not explicitly taken into account (see also Pattle et al. 2015).

2.2. Herschel observations

The *Herschel* SPIRE data at 250, 350, and 500 μm were taken from the *Herschel* Science Archive (HSA)[1]. We use the level 2.5 maps produced by the standard data reduction pipelines and calibrated for extended emission (the so-called Photometer Extended Map Product). The observations ID numbers are 1342204856 and 1342204857 and the data were originally observed in the HOBYS programme (Motte et al. 2010).

The resolutions of the SPIRE observations are 18.4″, 25.2″, and 36.7″ in the 250, 350, and 500 μm bands, respectively[2]. The beam sizes and shapes depend on the source spectrum[3]. We use beams that are calculated for a modified black-body spectrum with a colour temperature of T = 15 K and a dust emission spectral index of β = 1.8. The beam shapes are not sensitive to small variations in T and β (Griffin et al. 2013; Juvela et al. 2015a) but could be less accurate for hot point sources. We adopt for the SPIRE bands a relative uncertainty of 4%.

The surface brightness scale of the archived *Herschel* SPIRE maps have an absolute zero point that is based on a comparison with *Planck* measurements (e.g. Fig. 1). We convolved the maps to 40″ resolution, fitted the data with modified blackbody (MBB) curves with $\beta = 1.8$, and used these spectral energy distributions (SEDs) to colour correct the SPIRE and SCUBA-2 data. In the temperature range of $T = 10-20$ K, the corrections are less than 2%. For example, the SPIRE colour corrections remain essentially identical irrespective on whether the colour temperatures are estimated using the total intensity or the background-subtracted surface brightness data (see Sect. 4.1).

We show some *Herschel* maps from the PACS instrument (Poglitsch et al. 2010) but these data are not used in the analysis of dust emission. At 70 μm, the filament is seen in absorption (except for a number of point sources) and at 160 μm the filament is seen neither in absorption nor as an excess over the background (see Fig. 2). Even without this significant contribution of the extincted background component, the inclusion of shorter wavelengths would bias the estimates of the dust SED parameters (e.g. Shetty et al. 2009b; Malinen et al. 2011; Juvela & Ysard 2012b).

2.3. Other data on infrared and radio dust emission

Planck 850 μm (353 GHz) data are used to examine the dust emission and the dust polarisation at scales larger than the ∼5′ *Planck* beam. The data were taken from the Planck Legacy Archive[4] and correspond to the 2015 maps (Planck Collaboration I 2016) where the CMB emission has been subtracted. We make no corrections for the cosmic infrared background (CIB) because its effect (∼0.13 mJy sr^{-1} at 353 GHz; Planck Collaboration Int. XXIX 2016) is insignificant compared to the strong cloud emission. The *Planck* 850 μm data has some contamination from CO J = 3–2 line emission. We do not correct for this, because the effect is small and these data are not used for SED analysis (see also Juvela et al. 2015a). The estimated effect of the (unpolarised) CO emission on the polarisation fraction p is not significant, ∼1% or less of the p values.

[1] http://archives.esac.esa.int/hsa/whsa/
[2] The Spectral and Photometric Imaging Receiver (SPIRE) Handbook, http://herschel.esac.esa.int/Docs/SPIRE/spire_handbook.pdf.
[3] http://herschel.esac.esa.int/twiki/bin/view/Public/SpirePhotometerBeamProfileAnalysis
[4] https://www.cosmos.esa.int/web/planck/pla

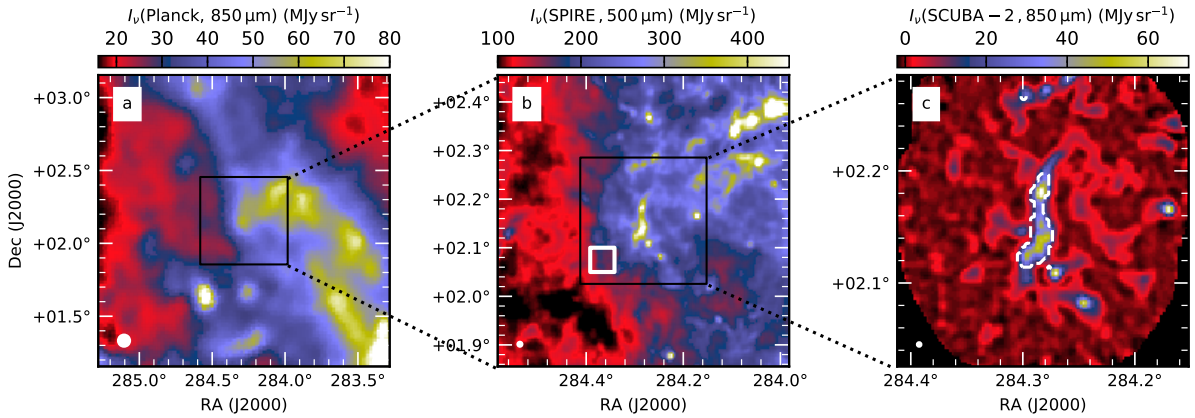

Fig. 1. *Planck* 850 μm (353 GHz), *Herschel* 500 μm, and SCUBA-2/POL-2 850 μm surface brightness maps of the G035.39-00.33 filament and its surroundings. The beam sizes are indicated in the lower left corner of each panel (5′, 37″, and 14″, respectively). In *panel b* the white box indicates a reference region for background subtraction. The dashed contour in *panel c* is drawn at the level of 180 mJy sr^{-1} of the background-subtracted 500 μm surface brightness.

Figure 1 shows *Planck*, *Herschel*, and SCUBA-2 surface brightness maps of the G035.39-00.33 region. Figure 2 shows surface brightness images from mid-infrared (MIR) to submillimetre wavelengths. In addition to *Herschel* data, the figure shows the 12 μm surface brightness from the WISE survey (Wright et al. 2010). The filament is seen in absorption up to the 70 μm band. The 160 μm image is dominated by warm dust and the main high-column-density structure is not visible, before again appearing in emission at 250 μm. The ratio of the 100 μm and 250 μm dust opacities is ∼5, which suggests (although does not directly prove) that the filament is optically thin at 250 μm. This is later corroborated by the derived τ(250 μm) estimates and by independent column density estimates.

The 70 μm image shows more than ten point-like sources that appear to be associated with the main filament. Only one of them is visible at 12 μm, showing that they are either in an early stage or otherwise heavily obscured by high column densities. The sources can be identified also in the PACS 160 μm image but not at 250 μm, because of the lower resolution and lower sensitivity to high temperatures, many of the sources are blended together or not visible above the extended cold dust emission. The sources were studied by Nguyen Luong et al. (2011), who also estimated their bolometric luminosities. The sources with luminosity (or with an estimated upper limit) above 100 $L_\odot$ are marked in Fig. 2b and are listed in Table 2. The numbering refers to that in Nguyen Luong et al. (2011) Table 1. The most luminous source No. 2 is outside the main filament. The others have bolometric luminosities of the order of 100 $L_\odot$. The low dust temperatures indicate that the internal heating caused by these (probably) embedded sources is not very significant.

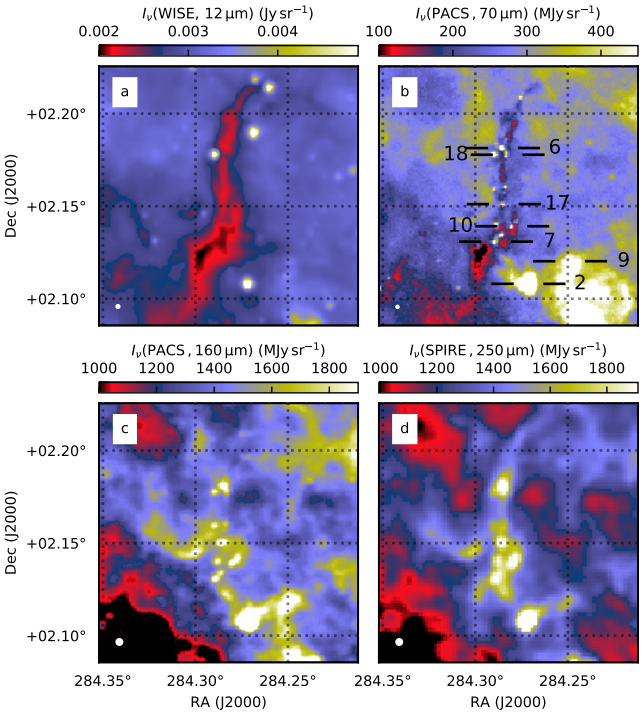

Fig. 2. WISE 12 μm, *Herschel* PACS instrument 70 and 160 μm, and SPIRE instrument 250 μm surface brightness images of G035.39-00.33. In the 70 μm image, some of the highest-luminosity sources from Nguyen Luong et al. (2011) are indicated.

2.4. Extinction data

Kainulainen & Tan (2013) calculated for the G035.39-00.33 region the high-dynamical-range extinction maps using a combination of NIR observations of reddened background stars and the MIR extinction of extended emission. A NIR extinction map was made at 30″ resolution using UKIDSS data (Lawrence et al. 2007) and an adaptation of the NICER method in Kainulainen et al. (2011; see also Lombardi & Alves 2001). The assumed extinction curve has τ(V) = 3.54 τ(J) (Cardelli et al. 1989). The MIR extinction was measured using Spitzer 8 μm images from the GLIMPSE survey (Butler & Tan 2012a). This enabled the extension of the estimates to higher column densities and down to a nominal resolution of 2″. The MIR data suffer from spatial filtering (low sensitivity to extended structures) and exhibit some differences relative to the NIR data that could be caused by fluctuations in the brightness of the background (or foreground). Kainulainen & Tan (2013) compensated for these effects by combining the two data sets into a single A_V map. The correlation between the NIR and MIR data was best in the A_V = 10 − 15 mag range while at higher column densities the NIR estimates are, as expected, smaller because the background stars do not provide a good sampling of the highest column densities. The morphology and relative extinction values in the combined extinction

Table 2. List of the most luminous sources in the G035.39-00.33 field.

No.[a]	RA (J2000)	Dec (J2000)	$T_{\rm dust}$ (K)	M ($M_\odot$)	L ($L_\odot$)
2	18:57:05.1	2:06:29	27 ± 6	24 ± 16	4700
6	18:57:08.4	2:10:53	16 ± 3	20 ± 12	70–200
7	18:57:09.3	2:07:51	12 ± 1	49 ± 17	50–130
9	18:56:59.7	2:07:13	22 ± 4	3 ± 1	70–120
17	18:57:08.3	2:09:04	13 ± 2	50 ± 19	50–140
18	18:57:07.8	2:10:40	14 ± 2	20 ± 9	40–120

Notes. [(a)]Source numbering from the Table 1 of Nguyen Luong et al. (2011).

map are not dependent on a priori assumptions of the absolute dust opacities but do depend on the assumed opacity ratio of $\kappa(8\mu{\rm m})/\kappa({\rm K}) = 0.29$.

We converted the Kainulainen & Tan (2013) $A_{\rm V}$ estimates (data provided by J. Kainulainen) to J band optical depth $\tau({\rm J})$ using the opacity ratio quoted above. In Sect. 4.3 the $\tau({\rm J})$ map will be compared to observations of dust emission.

3. Methods

3.1. Column density estimates

Basic column density estimates can be derived via modified black-body (MBB) fits that model the observed intensities as

$$I_\nu(\nu) = I_\nu(\nu_0)\frac{B_\nu(\nu,T)}{B_\nu(\nu_0,T)}\left(\frac{\nu}{\nu_0}\right)^\beta, \quad (1)$$

where B_ν is the Planck law, T the colour temperature, β the dust opacity spectral index, $I_\nu(\nu)$ the observed intensities, and $I_\nu(\nu_0)$ the intensity at the reference frequency ν_0. In the MBB fit, the free parameters are $I_\nu(\nu_0)$, T, and β, although in many cases the spectral index β is kept fixed. With an assumption of the value of $\kappa(\nu_0)$, the dust opacity relative to the total gas mass, the MBB result can be converted to estimates of the column density,

$$N({\rm H}_2) = \frac{I_\nu(\nu_0)}{B_\nu(T)\kappa(\nu_0)\mu m_{\rm H}}. \quad (2)$$

Here μ is the total mass per hydrogen molecule, $\mu = 2.8$ in atomic mass units. The mass surface density ($\rm g\,cm^{-2}$) is $\Sigma = N({\rm H}_2)\mu$. We adopt dust opacities $\kappa(\nu) = 0.1\,(\nu/1000\ {\rm GHz})^\beta\ {\rm cm^2\,g^{-1}}$ (Beckwith et al. 1990; Juvela et al. 2012). The above assumes that the observed intensities can be represented by a single MBB formula like in Eq. (1). This is not generally true and, in particular, leads to an underestimation of the column densities of non-isothermal sources (Shetty et al. 2009b; Malinen et al. 2011; Juvela & Ysard 2012b; Juvela et al. 2013a). Equation (1) also explicitly assumes that the emission is optically thin, which is probably the case for G035.39-00.33 observations at wavelengths $\lambda \geq 250\,\mu$m. For optically thick emission, the column density estimates would always be highly unreliable and the use of the full formula instead of the optically thin approximation of Eq. (1) is not likely to improve the accuracy (Malinen et al. 2011; Men'shchikov 2016).

If all the maps used in the fits are first convolved to a common low resolution, the previous formulas provide column density maps at this resolution. We also made column density maps at a higher resolution by making a model that consisted of high-resolution $I_\nu(\nu_0)$ and T maps, keeping the spectral index β constant. This model provides predictions at the observed frequencies according to Eq. (1). Each model-predicted map was convolved to the resolution of the corresponding observed map using the convolution kernels described in Sects. 2.1 and 2.2. The minimisation of the weighted least squares residuals provided the final model maps for $I_\nu(\nu_0)$ and T. The free parameters thus consisted of the intensity values $I_\nu(\nu_0)$ and the temperature values T of each pixel of the model maps. The chosen pixel size was 6″, more than two times smaller than the resolution of the observed surface brightness maps. Because the solution at a given position depends on the solution at nearby positions, the $I_\nu(\nu_0)$ and T maps need to be estimated through a single optimisation problem rather than for each pixel separately. The optimised model maps were convolved to $FWHM_{\rm MOD}$ and were then used to calculate column density maps at that same resolution. We used $FWHM_{\rm MOD} = 20''$, when fitting *Herschel* data, and $FWHM_{\rm MOD} = 15''$, when fitting combined *Herschel* and SCUBA-2 observations. The procedure is discussed further in Appendix A. Because the method is simply fitting the observed surface brightness values, it is still subject to all the caveats regarding the line-of-sight (LOS) temperature variations.

3.2. Polarisation quantities

The polarisation fraction could be calculated as

$$p = \frac{\sqrt{Q^2+U^2}}{I}, \quad (3)$$

but this estimate is biased because of observational noise and because p depends on the squared sum of Q and U. Therefore, we use the modified asymptotic estimator of Plaszczynski et al. (2014),

$$p_{\rm mas} = p - b^2\frac{1-\exp(-p^2/b^2)}{2p}, \quad (4)$$

where b^2 is

$$b^2 = \frac{\sigma'^2_U\cos^2(2\psi_0-\theta)+\sigma'^2_Q(2\psi_0-\theta)}{I_0^2}, \quad (5)$$

with

$$\theta = \frac{1}{2}{\rm atan}\left(\frac{2\sigma_{QU}}{\sigma_Q^2-\sigma_U^2}\right), \quad (6)$$

$$\sigma'^2_Q = \sigma_Q^2\cos^2\theta + \sigma_U^2\sin^2\theta + \sigma_{QU}\sin 2\theta, \quad (7)$$

$$\sigma'^2_U = \sigma_Q^2\sin^2\theta + \sigma_U^2\cos^2\theta - \sigma_{QU}\sin 2\theta. \quad (8)$$

In Eq. (5) ψ_0 stands for the true polarisation angle and is in practice replaced by its estimate (see below). The error estimates of p are calculated from

$$\sigma_{p,\,\rm mas} = \sqrt{\sigma'^2_Q\cos^2(2\psi-\theta)+\sigma'^2_U\sin^2(2\psi-\theta)}/I \quad (9)$$

(Plaszczynski et al. 2014; Montier et al. 2015b). The $p_{\rm mas}$ estimator is reliable at $p_{\rm mas}/\sigma_{p,{\rm mas}} > 2$ (Montier et al. 2015b). In this

paper, polarisation fractions are calculated using the $p_{\rm mas}$ estimator, both in the case of real observations and in the simulations of Appendix C. The only exception is the analysis of radiative transfer models (Sect. 5), because these are free of noise that could affect the p estimates.

The polarisation angle depends on Stokes Q and U as

$$\psi = 0.5 \arctan(U, Q). \tag{10}$$

We use the IAU convention where the angle increases from north towards east. The estimated POS magnetic field orientation is obtained by adding $\pi/2$ rad to ψ. The uncertainties of ψ are estimated as

$$\sigma_\psi = \sqrt{\frac{Q^2\sigma_U^2 + U^2\sigma_Q^2 - 2QU\sigma_{QU}}{Q^2\sigma_Q^2 + U^2\sigma_U^2 + 2QU\sigma_{QU}}}\ \frac{\sigma_p}{2p}\ \text{rad}, \tag{11}$$

based on the error estimates of the Stokes parameters σ_Q and σ_U and the covariance between Stokes Q and U, σ_{QU} (Plaszczynski et al. 2014; Montier et al. 2015b). All the quantities in the above formulas are available from the data reduction except for the SCUBA-2 covariances σ_{QU}, which are set to zero. Montier et al. (2015a) note that the ψ error estimates are reliable for $S/N > 4$ but can be strongly underestimated for lower S/N because of the bias of the p parameter.

The uniformity of the polarisation vector orientations and thus the regularity of the underlying magnetic field can be characterised with the polarisation angle dispersion function S (Planck Collaboration Int. XIX 2015). It is calculated as a function of position $\bar{r}$ as

$$S(\bar{r}, \bar{\delta}) = \sqrt{\frac{1}{N}\sum_{i=1}^{N}\left(\psi(\bar{r}) - \psi(\bar{r} + \bar{\delta}_i)\right)^2}. \tag{12}$$

Here $\bar{\delta}_i$ is an offset for N map pixels at distances $[\delta/2, 3\delta/2]$ from the central position $\bar{r}$. The scalar δ thus defines the spatial scale at which the dispersion is estimated. We set the δ values according to the present data resolution as $\delta = FWHM/2$. The angle difference is calculated directly from the Stokes parameters as

$$\psi(\bar{r}) - \psi(\bar{r} + \bar{\delta}_i) = \arctan(Q_r U_\delta - Q_\delta U_r, Q_r Q_\delta + U_r U_\delta)/2, \tag{13}$$

where the indices r and δ refer to the positions $\bar{r}$ and $\bar{r} + \bar{\delta}_i$, respectively. In the convolution of the Stokes vector images and in the calculation of the polarisation angle dispersion function, we take into account the rotation of the polarisation reference frame as described in Appendix A of Planck Collaboration Int. XIX (2015). However, these corrections are not very significant at the angular scales discussed in this paper. All S values presented in this paper are bias-corrected as $\sqrt{S^2 - \sigma(S)^2}$, where $\sigma(S)$ is the estimated uncertainty for S in Eq. (12) (Planck Collaboration Int. XIX 2015).

3.3. Radiative transfer models

We complemented the analysis described in Sects. 3.1 and 3.2 with radiative transfer (RT) calculations. These have the advantage of providing a more realistic description of the temperature variations and, in the case of polarisation, allow the explicit testing of the effects of imperfect grain alignment and different magnetic field geometries.

The models cover an area of $13' \times 13'$ on the sky with a regular grid where the size of the volume elements corresponds to $6''$. The LOS density profile was assumed to have a functional form of $n(z) \propto (1 + (z/R)^2)^{p/2}$, where z is the LOS coordinate. With parameters $R = 0.16$ pc and $p = 2$, this gives for the filament similar extent in the LOS direction as observed in the POS. Such a short LOS extent is appropriate only for the densest regions. Therefore, we used a scaled LOS coordinate z/z_N where z_N is linear with respect to the logarithm of the column density and increases from one for $N > 5 \times 10^{22}$ cm^{-2} to five for a factor of 10 smaller column densities.

The RT model initially corresponded to the column densities estimated from MBB fits at $40''$ resolution. The cloud was illuminated by the normal interstellar radiation field (ISRF) according to the Mathis et al. (1983) model. The dust properties were taken from Compiègne et al. (2011) but the dust opacity at wavelengths $\lambda > 100\,\mu$m were increased to give $\tau(250\,\mu\text{m})/\tau(\text{J})$ ratios of 10^{-3} or 1.6×10^{-3}. The extinction curve was rescaled to give the same $\kappa(250\,\mu\text{m})$ value as quoted in Sect. 3.1. The latter scaling has no real effect on the RT modelling itself but simplifies the comparison with values derived from observations.

The models were optimised to match a set of surface brightness observations. The free parameters included the scaling of the column densities, one parameter per a $6''$ map pixel, and the scaling of the external radiation field, $k_{\rm ISRF}$. The G035.39-00.33 region includes a number of radiation sources with luminosities $\sim 10\,L_\odot$ or less. Because their location along the line of sight is not known, the qualitative effects of internal heating were tested by including in the model an optional diffuse emission component. The diffuse emission has the same spectrum as the external radiation field and it was scaled with a parameter $k_{\rm diff}$, the value of 1 corresponding to a bolometric luminosity of $1\,L_\odot\,\text{pc}^{-3}$.

The radiative transfer problem was solved with the Monte Carlo programme SOC (Juvela 2018; Gordon et al. 2017). Because the fitted observations are at long wavelengths $\lambda \geq 250\,\mu$m, the dust grains were assumed to be in equilibrium with the radiation field and the emission from stochastically heated grains was omitted. SOC calculates the dust temperatures based on the radiative transfer simulation and writes out surface brightness maps at the requested wavelengths.

SOC can be used to calculate estimates of the polarised dust emission. This was done using grain alignment that was either constant, had an ad hoc density dependence, or was predicted by RAT calculations (Lazarian & Hoang 2007). For the RAT case, the radiative transfer modelling provided the intensity and anisotropy of the radiation field, which were then used to estimate the minimum size of aligned grains and thus a reduction factor R for the polarised emission originating in each model cell. The calculations were done as described in Pelkonen et al. (2009). The polarisation signal is dependent on the minimum size of the grains that remain aligned in a magnetic field. This is dependent on the ratio between the angular velocity produced by the radiation field and the thermal rotation rate:

$$\left(\frac{\omega_{\rm rad}}{\omega_{\rm T}}\right)^2 \propto \frac{a}{(n_{\rm H}T)^2}\left[\int (Q_\Gamma \cdot \hat{a})\lambda J_\lambda \mathrm{d}\lambda\right]^2, \tag{14}$$

where $n_{\rm H}$ is the volume density, T the temperature, a the grain size, Q_Γ the wavelength-dependent efficiency of RAT (dependent on the grain properties), $\hat{a}$ the unit vector of the rotational axis, and J_λ the radiation field intensity. Thus, grain alignment is promoted by larger grain sizes and larger intensity and anisotropy of the radiation field. Conversely, higher density and temperature tend to reduce the grain alignment and subsequently the polarised intensity.

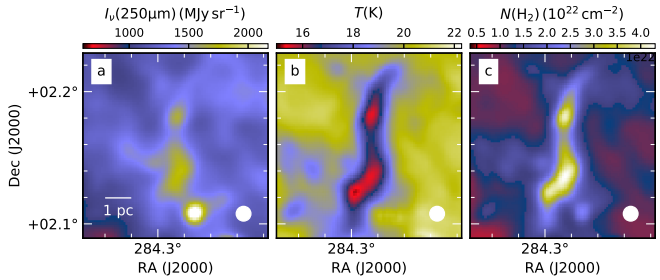

Fig. 3. Results of modified black-body fits to SPIRE data at 40″ resolution and without background subtraction: 250 μm intensity (*panel a*), colour temperature (*panel b*), and column density (*panel c*).

Given a model of the 3D magnetic field within the model volume, SOC gives synthetic maps for I, Q, and U. We used these to examine the effect that imperfect grain alignment can have on the observed polarisation fraction distributions. For comparison with the full calculations with grain alignment, synthetic maps were also produced assuming a constant value of R or an ad hoc density dependence of R.

4. Results

4.1. Herschel data

Figure 3 shows the results of MBB fits using SPIRE surface brightness maps at 40″ resolution. The fits were done to data before background subtraction and thus correspond to emission from the full LOS. The extended cloud component has a significant contribution of almost $N(\mathrm{H_2}) = 10^{22}\,\mathrm{cm^{-2}}$ to the total column density. The peak column densities of both the northern and the southern parts are $N(\mathrm{H_2}) \sim 4 \times 10^{22}\,\mathrm{cm^{-2}}$. The colour temperatures are 20–21 K in the background, below 18 K within the dense filament ($N(\mathrm{H_2}) > 2 \times 10^{22}\,\mathrm{cm^{-2}}$), and reach minimum values of 15.5 and 15.2 K in the northern and southern clumps, respectively. PACS data were not used (see Sect. 2.2), but at the temperatures of the main filament ($T \sim 15$ K), the *Herschel* 250, 350, and 500 μm SPIRE bands give reliable measurements of the dust colour temperature (see Juvela et al. 2012). On the other hand, they do not give strong simultaneous constraints for both the colour temperature and the spectral index. Therefore, the SPIRE data were fitted using a constant value of $\beta = 1.8$.

We created column density maps at a resolution of 20″, as described in Sect. 3.1 using background-subtracted data. The background was determined as the average signal in a $3' \times 3'$ area centred at RA = $18^{\mathrm{h}}57^{\mathrm{m}}28^{\mathrm{s}}$, Dec = 2°4′30″ (see Fig. 1b). Compared to Fig. 3, the filament is colder, mainly because of the background subtraction (see Fig. 4). The minimum temperatures are 12.4 K in the northern part and 11.7 K in the southern part (13.7 and 12.7 K, respectively, if this map is convolved down to 40″ resolution). At the 20″ resolution, the fitted I_ν (250 μm) map shows local maxima at the positions of the MIR sources (Fig. 2b) but are not similarly visible in column density. In spite of the background subtraction, the peak column densities are higher, slightly above $5 \times 10^{22}\,\mathrm{cm^{-2}}$ in both the northern and the southern parts. This is a consequence of the lower colour temperatures. The column densities are probably still underestimated because of LOS temperature variations. We will refer to this version of the column density map as $N_3(\mathrm{H_2})$, the sub-index referring to the number of bands fitted.

Unlike in the standard MBB fits that are done for each pixel separately, Fig. 4 corresponds to a global fit over the map. The fit residuals (Figs. 4d–f) are dominated by small-scale artefacts (below the beam size) that are connected with the finite pixel size and possibly with imperfections in the beam model. If these residual maps are convolved to the resolution of the observations, they are smooth with peak-to-peak errors below ∼4%.

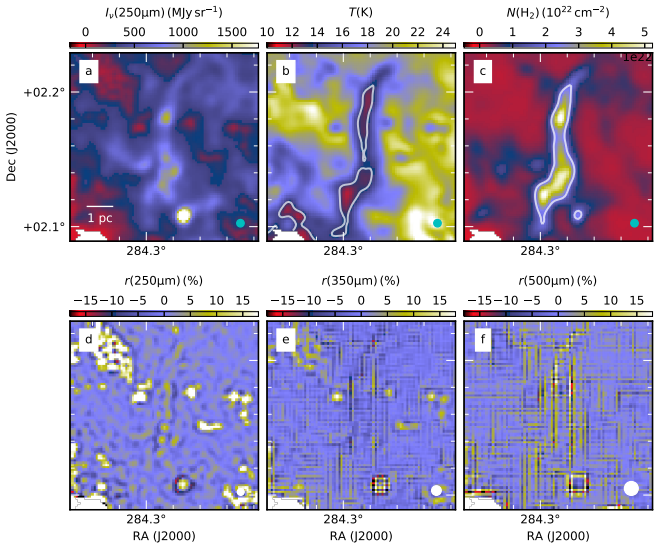

Fig. 4. Results of modified black-body fits to SPIRE data at a resolution of 20″. The *upper panels* show the fitted 250 μm intensity, dust colour temperature, and column density. The *lower panels* show the relative error of the fits for the individual SPIRE bands. We have masked a region in the SE corner where the background-subtracted 250 μm intensities are below 10 mJy sr^{-1}. The beam sizes of the observations are shown in the bottom right-hand corner of each panel. The contours are drawn at $T = 13.5$ K and $N(\mathrm{H_2}) = 2 \times 10^{22}\,\mathrm{cm^{-2}}$.

4.2. Combined Herschel and SCUBA-2 data

We estimated the average SED of the main filament using band-to-band correlations. We selected data where the background-subtracted SPIRE 500 μm values were above of 180 mJy sr^{-1} (see Fig. 1c), further dividing the filament into a northern and a southern part along $\delta = 2°10'$. The data were convolved to the resolution of the 500 μm band, each band was correlated with the 350 μm data, and the uncertainties of the linear fits were estimated with bootstrapping. The correlations in the northern and the southern regions and the SED fit to the combined data are shown in Fig. 5.

The data were fitted with MBB functions using the Markov chain Monte Carlo method and flat priors with temperatures in the range 7–30 K and spectral indices in the range 0.5–3.5. Fits to all five bands gave $T = 11.29 \pm 0.83$ K, $\beta = 2.06 \pm 0.22$ for the southern part, $T = 12.46 \pm 0.95$ K, $\beta = 1.82 \pm 0.24$ for the northern part, and $T = 11.92 \pm 0.87$ K, $\beta = 1.94 \pm 0.22$ for the combined data. In this last case, the fitted SED consisted of the weighted average of the SEDs points of the southern and northern parts. The effects from the spatial filtering of the SCUBA-2 data should be small because the selected data only cover a ∼1.5′ wide part of the filament. The 450 μm SCUBA-2 point of the northern region is significantly above the fitted SED. However, if this point is omitted, the spectral index estimate remains almost unchanged, $\beta = 1.95$. The fit to the three SPIRE channels without SCUBA-2 data gave $T = 12.66 \pm 1.42$ K, $\beta = 1.76 \pm 0.33$.

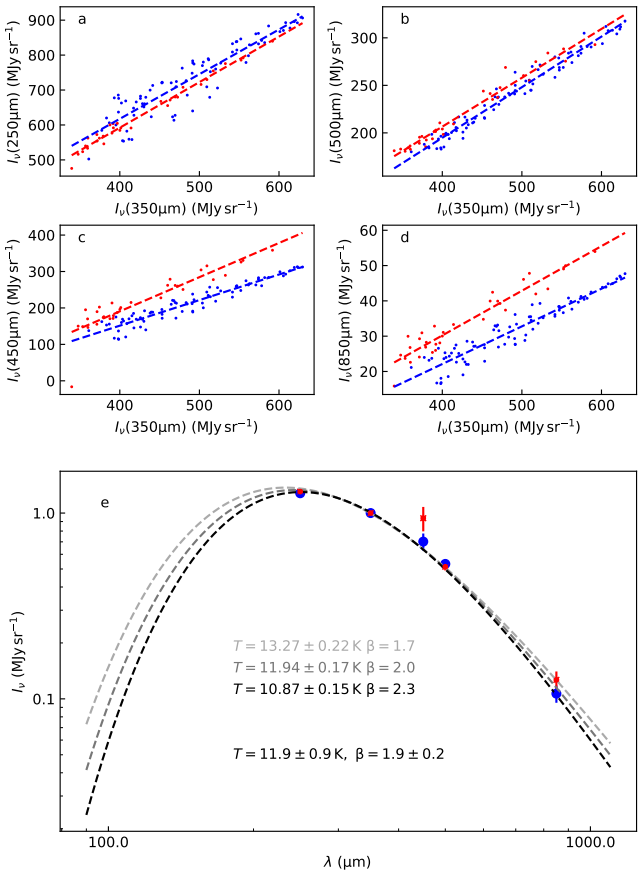

Fig. 5. SEDs from the correlations of surface brightness values over the main filament. *Panels a–d* show the band-to-band correlations for the northern (red) and southern (blue) parts of the filaments. The points correspond to an oversampling by a factor of 2 relative to the data resolution. *Panel e* shows the resulting SEDs and modified black-body fits to the combined data for three fixed values of the spectral index β. The result for a fit with free β are shown below the results of the fixed-β fits.

We fitted the SPIRE and the 850 μm data also with a model that had one free parameter for β, one free parameter for the relative offset of the 850 μm surface brightness map, and one free parameter for the colour temperature in each pixel. We used the same relative uncertainties as above but further assumed a correlation $\rho = 0.5$ between the errors of the SPIRE channels. Unlike in the previous surface brightness correlations, the fit relies on the consistency of the intensity zero points of the background-subtracted SPIRE maps. The results from Markov chain Monte Carlo calculations were $\beta = 1.84 \pm 0.02$ for the southern part and $\beta = 1.69 \pm 0.02$ for the northern part. These are close to the SPIRE-only fits, partly because the SCUBA-2 data have less leverage on the β values once the 850 μm surface brightness offset is included as a separate free parameter. All error estimates above correspond to the 4% (SPIRE) and 10% (SCUBA-2) uncertainties of the surface brightness measurements. The true uncertainties can be larger because of the systematic errors.

We fitted the three SPIRE and two SCUBA-2 bands together to derive maps of dust colour temperature and of optical depth at 15″ resolution, under the assumption of $\beta = 1.8$. The optimisation procedure is the same as in Sect. 4.1 (see Sect. 3.1). We used background-subtracted SPIRE data but also had to correct the zero points of the SCUBA-2 data. This was done by taking the predictions of SPIRE fits with $\beta = 1.8$ at the wavelengths 450 and 850 μm and comparing these to the SCUBA-2 maps at the same resolution. The 450 μm offset was calculated using the average surface brightness values of the pixels where the original SCUBA-2 450 μm value was above 160 mJy sr^{-1}. For the 850 μm map, the corresponding threshold was 30 mJy sr^{-1}. These offset-corrected maps were used as additional constraints in the area where the signal was above the quoted surface brightness thresholds. This means that SCUBA-2 data were used over a narrow region around the main filament where the loss of low spatial frequencies should be small. Because the offsets were based on the SPIRE SEDs, these data cannot be used to draw any conclusions on the SED shape at wavelengths beyond 500 μm. The SCUBA-2 data only provide additional constraints on the small-scale column density structure. The resulting 250 μm optical depth estimates are referred to as τ_5 (250 μm) and the column density estimates as $N_5(H_2)$.

The results are shown in Fig. 6 at the resolution of *FWHM* = 15″ (Gaussian beam). In principle, this is the resolution also outside the main filament, where SCUBA-2 data were not used. However, there *FWHM* = 15″ corresponds to a deconvolution below the SPIRE resolution and the small-scale structure is not reliable. The peak column densities are 7.2×10^{22} and 7.0×10^{22} cm^{-2} for the northern and southern parts, respectively. Unlike in Fig. 4, there are several local column density maxima NW of the southern clump that are related to the 70–250 μm sources of Fig. 2. They are more visible because of the higher resolution (15″ vs. 20″). However, if the effective resolution of the fitted temperature map (which is dependent on longer-wavelength SPIRE channels) is lower than the effective resolution of the fitted surface brightness map, the column density estimates could be biased upwards at the location of warm point-like sources.

4.3. Dust opacity

The extinction map of Kainulainen & Tan (2013; Sect. 2.4) enables us to compare dust opacities between the NIR/MIR and sub-millimetre regimes. The correlations of these τ(J) values with the τ_5 (250 μm) optical depth estimates are shown in Fig. 7.

The least squares fit gave an average ratio of $\tau(250\ \mu\text{m})/\tau(\text{J}) = (2.55 \pm 0.03) \times 10^{-3}$. The error estimate only refers to the uncertainty of the fit itself, which was estimated by bootstrapping. The relation is found to be steeper in the northern clump and shallower for $\tau(\text{J}) < 6$ (see Fig. 7).

In addition to the correlation plot of Fig. 7, we estimated the $\tau(250\ \mu\text{m})/\tau(\text{J})$ ratio based on the absolute values. We subtracted from the τ(J) and τ(250 μm) maps a background that was estimated as the average along a 1′-wide boundary that follows the contour in Fig. 7a. After the subtraction of the local background, the average values inside the contour gave $\tau(250\ \mu\text{m}))/\tau(\text{J}) = (2.1 \pm 0.5) \times 10^{-3}$. The error estimate is based on the total signal fluctuations over the area used for background subtraction.

4.4. Polarisation data

Figure 8 shows an overview of the *Planck* and POL-2 polarisation data. *Planck* maps have very little noise. When POL-2 data are convolved to a 40″ resolution, the polarisation angle dispersion *S* is clearly affected by noise outside the $N(H_2) = 10^{22}$ cm^{-2} contour and *p* becomes dominated by noise closer to the map edges. At the higher 20″ resolution, polarisation fraction values become uncertain as soon as column density drops below $N(H_2) = 10^{22}$ cm^{-2}.

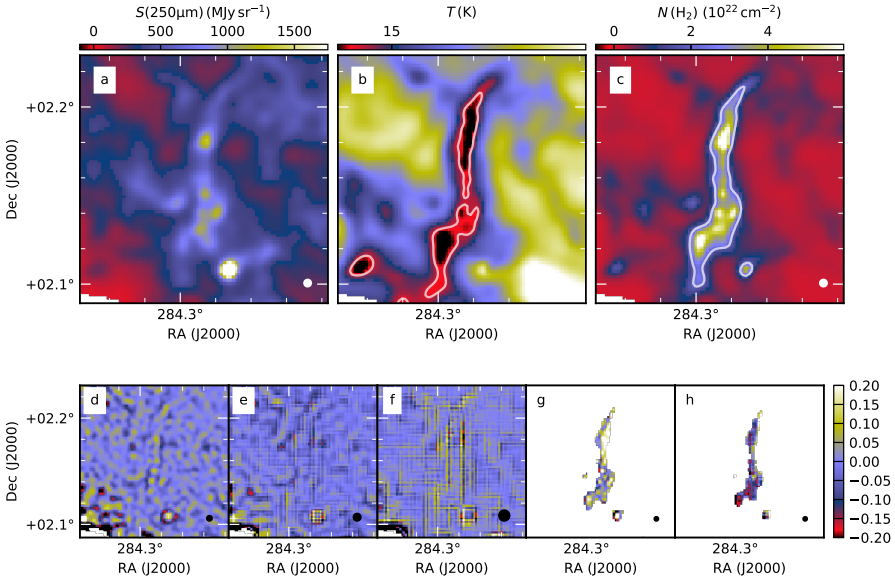

Fig. 6. Modified black-body fit to the combined SPIRE and SCUBA-2 data at 15″ resolution, using SCUBA-2 data as a constraint only over the main filament. *Panels a–c*: the fitted 250 μm surface brightness, the colour temperature, and the estimated column density, respectively. *Panels d–h*: the residuals relative to the observed, background-subtracted surface brightness values at 250, 350, 500, 450, and 850 μm, respectively. The fits used $\beta = 1.8$. The contours are drawn at $T = 13.5$ K and $N(H_2) = 2 \times 10^{22}$ cm^{-2}.

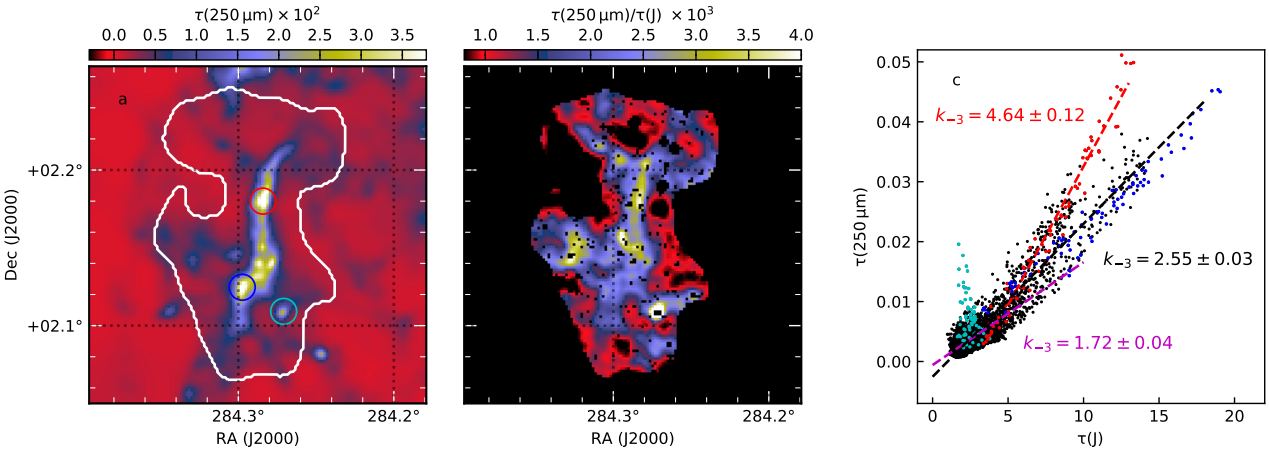

Fig. 7. Comparison of τ (250 μm) and τ (J) estimates: the τ (250 μm) map (*panel a*), the ratio $k_{-3} = 10^{-3} \times \tau(250\,\mu\text{m})/\tau(\text{J})$ (*panel b*), and the same ratio as a correlation plot (*panel c*). The last two panels are limited to data in the area indicated in the first panel, also excluding pixels for which τ (J) is not defined because of masked stars. Selected 30″ radius regions (see *panel a*) are marked in *panel c* with different colours: a point source SE of the southern clump (cyan) and the northern and southern τ (250 μm) peaks (red and blue circles, respectively). The black line in *panel c* is a least squares fit to the data, only excluding the SE point source. Fits to the northern clump and to data τ (J) < 6 are shown in red and magenta, respectively.

Figure 9 shows histograms for the S/N of polarisation fraction, $p_{\rm mas}/\sigma_{p,\rm mas}$. The plot includes histograms for *Planck* data at 5′ resolution and for the POL-2 data at 20″ and 40″ resolutions. According to Montier et al. (2015b), $p_{\rm mas}$ is unbiased for $p_{\rm mas}/\sigma_{p,\rm mas} > 2$. The S/N is sufficient for almost all *Planck* data at the full resolution and most of the POL-2 data at 40″ resolution, when selected at $N(H_2) > 10^{22}$ cm^{-2}. Data cannot be thresholded directly using the S/N because that would lead to a biased selection of p values (Planck Collaboration XII 2018). Figure 9c shows that at 20″ resolution a significant part of POL-2 $p_{\rm mas}$ estimates may be biased (at $S/N < 2$ the modified asymptotic estimator may not remove all the bias in p) and a higher column density threshold does not fully remove the problem.

The polarisation angle estimates are mainly unbiased but since they are affected by noise, at low S/N the polarisation angle dispersion function S will have systematic positive errors that are not fully removed by the bias correction. The appearance of the Fig. 8 maps is in qualitative agreement with this.

4.5. Magnetic field geometry

The magnetic field geometry of the cloud G035.39-00.33 has been discussed in detail in Liu et al. (2018b) based on the POL-2 observations. However, we present some plots on the magnetic field morphology before concentrating on the polarisation fraction in the following sections.

Figure 10a shows a large-scale polarisation map based on *Planck* 850 μm. This is dominated by a regular field that in equatorial coordinates runs from NE to SW. At the 5′ resolution, the G035.39-00.33 filament is not prominent because of the strong background emission (see Fig. 1). The SCUBA-2 850 μm surface brightness map in Fig. 11a shows the main ridge and some other filamentary features that were discussed in Liu et al. (2018b). At this 14″ resolution, the polarisation vectors show a less ordered field. In the central part, the field is partly perpendicular to the filament. In the north, the field turns parallel to the filament and is thus almost perpendicular to the large-scale field observed by *Planck*. The SE–NW

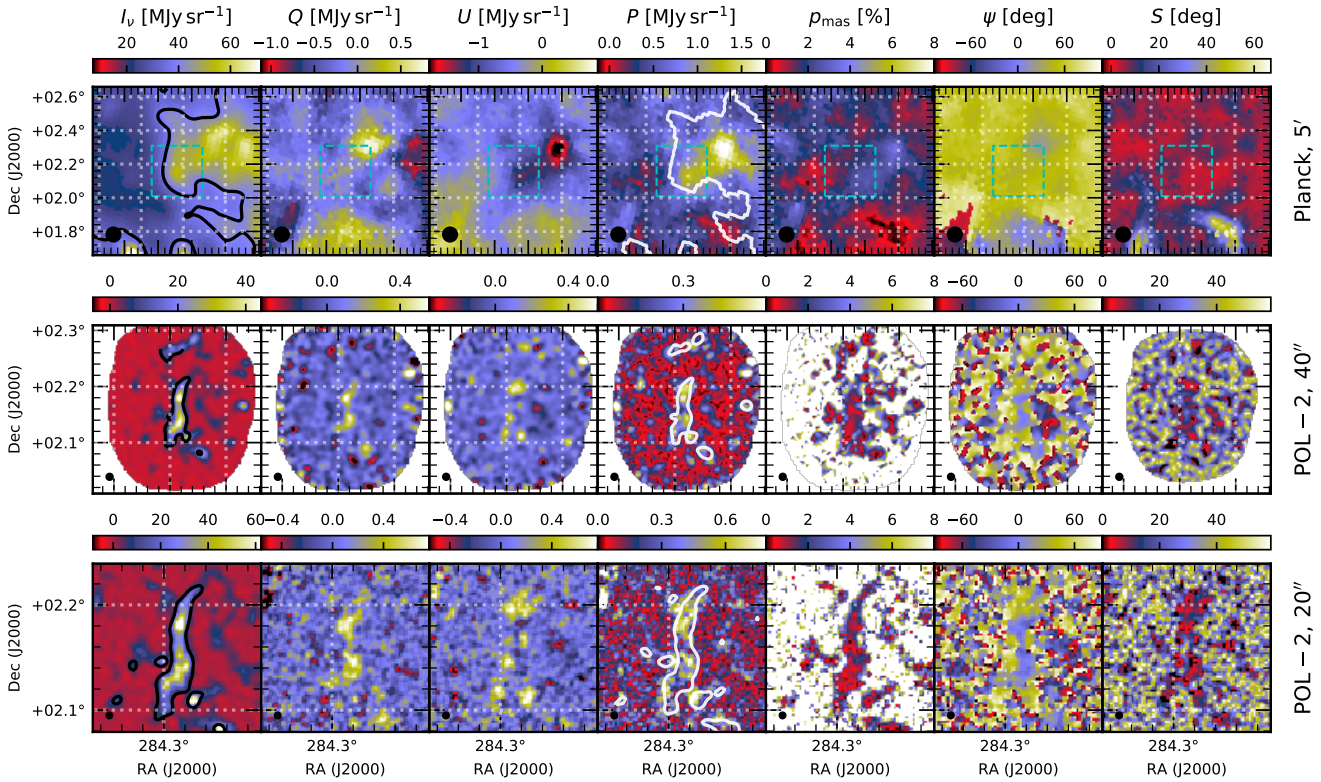

Fig. 8. Overview of polarisation data of the G035.39-00.33 region. The three rows show, respectively, *Planck* data at 5′ resolution, POL-2 data at 40″ resolution, and POL-2 data at 20″ resolution. The seven frames on each row are: I, Q, U, polarised intensity P, polarisation fraction $p_{\rm mas}$, polarisation angle ψ, and polarisation angle dispersion function S for a lag of δ = *FWHM*/2. The dashed boxes on *Planck* maps correspond to the size of the second row images. The column densities $N(H_2) = 10^{22}$ cm^{-2} (at the corresponding resolutions) are indicated with contours on the I maps. On the second and third rows, these are calculated from background-subtracted *Herschel* and SCUBA-2 data. The white contours on the P maps correspond to an intensity $I(850\mu{\rm m})$ of 40 mJy sr^{-1} on the *Planck* map and 10 mJy sr^{-1} on the POL-2 maps.

orientation observed in the northern end is actually common to filament boundary regions and is particularly clear on the eastern side.

The second panels in Figs. 10 and 11 show maps of the bias-corrected polarisation angle dispersion function S. For *Planck*, these are calculated at the scale of δ = 2.5′ using the *Planck* observations at their native resolution of *FWHM* = 5′. In the case of SCUBA-2, to increase the S/N, the data were smoothed to a resolution of 40″ and S was calculated with δ = 20″. Figure 11 shows that in POL-2 observations $S(20'')$ goes in some areas below ∼10°. Higher values are found, for example, in the northern clump. There the change in the magnetic field orientation coincides with the intensity maximum and large S values are not produced by noise alone. Similarly, at the eastern filament edge, the polarisation angles are uniform along the boundary but change systematically between the high and low column densities, contributing to the variation seen inside the $N(H_2) = 10^{22}$ cm^{-2} contour.

The *Planck* polarisation vectors are quite uniform over the G035.39-00.33 filament while the field geometry in SCUBA-2 850 μm data is different and partly orthogonal. One may ask whether the observations are consistent or whether the locally changing magnetic field orientation should be visible in *Planck* data as a drop in the polarisation fraction. We tested this by making simultaneous fits to the I, Q, and U data of both *Planck* and SCUBA-2. The results in Appendix B show that the observations are not contradictory. This is possible because of the large difference in the beam sizes and because the SCUBA-2 data are not sensitive to emission at scales larger than 200″. Thus, most information about the large-scale field is filtered out in the SCUBA-2 data.

4.6. Polarisation fraction

4.6.1. Polarisation fraction from *Planck* observations

Figure 12 shows the bias-corrected polarisation fraction estimate $p_{\rm mas}$ from *Planck* observations over a 1° × 1° region and at a resolution of 5′. The average value is $p \sim 2\%$. For comparison, the *Herschel* column density map was convolved to the same resolution but the polarisation fraction does not show clear dependence on the column density. At this resolution, the G035.39-00.33 filament shows up in the column density map only as a minor local maximum and the polarised signal appears to be dominated by more extended emission components. The polarisation fraction values at the filament location are slightly higher than in the region on average, close to 2.5%, as indicated in Fig. 12d.

We examine in Fig. 13 how, in the case of *Planck* data, the bias-corrected polarisation fraction and the estimated polarisation angle dispersion function depend on the column density and on the data resolution. The changes from 5′ to 9′ and further to 15′ resolution each correspond to about a factor of 3 increase of S/N. Irrespective of the resolution (and S/N), the mode of S is close to 10% and the values in area covered by SCUBA-2 are of similar magnitude. The polarisation fraction is mainly between 0.5 and 3% and there is no significant difference between the 9′ and 15′ resolution cases. The p values within

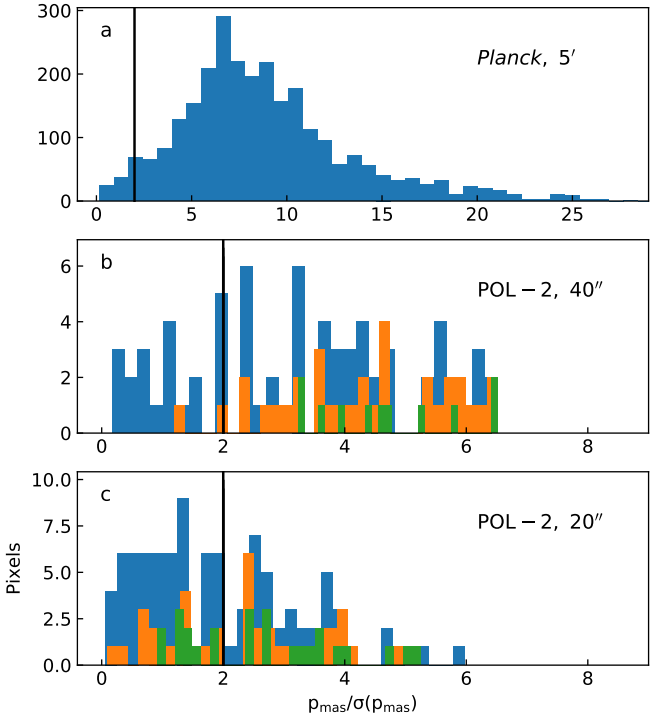

Fig. 9. S/N of polarisation fraction. The panels correspond to *Planck* data at 5′ resolution (*panel a*) and to POL-2 data at 40″ (*panel b*) and 20″ (*panel c*) resolution. *Panel a* includes all data over a 2° × 2° area. In *panels b and c*, histograms show POL-2 data above column density thresholds of 1, 2, and 3 times $N(H_2) = 10^{22}$ cm^{-2} (blue, orange, and green histograms, respectively). Vertical lines at 2 indicate an approximate limit above which the p_{mas} estimates are reliable. All data are sampled at steps *FWHM*/2.

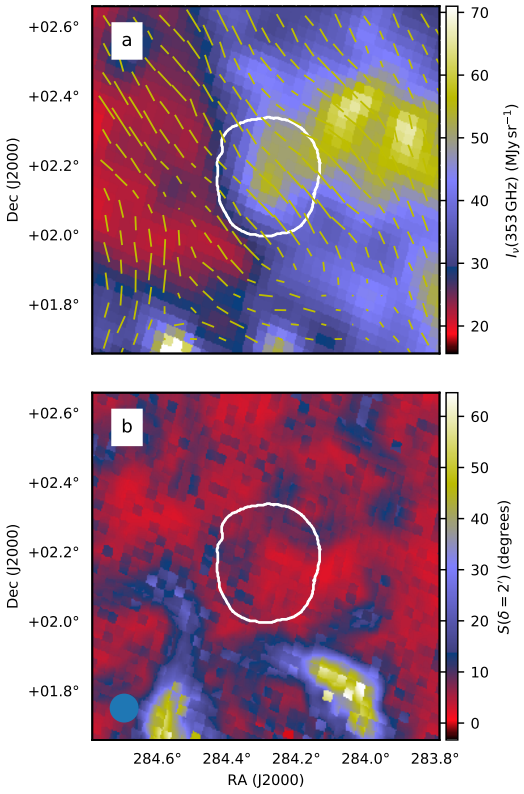

Fig. 10. *Planck* 850 μm (353 GHz) surface brightness with vectors showing the POS magnetic field orientation (*panel a*) and polarisation angle dispersion function $S(\delta = 2.5')$ calculated from *Planck* data (*panel b*). The maps are at the original 5′ resolution. The white contours indicate the area covered by SCUBA-2 observations. The length of the polarisation vectors is proportional to the polarisation fraction (90″ for 1% of polarisation).

the area mapped with SCUBA-2 are higher than on average, 2–2.5% for the full-resolution data and ~2% at lower resolutions. In the same region, S tends to be lower than average. This anti-correlation between p and S is clear in Fig. 13c. This could have its origin in either the noise (which increases the estimates of both quantities) or in the magnetic field geometry. The effects of noise has been characterised in previous *Planck* studies (Planck Collaboration Int. XIX 2015), and should here be small when data are smoothed to increase the S/N. The relation are similar for *FWHM* = 9′ and *FWHM* = 15′, which shows that the results are not severely affected by noise. This is confirmed with simulations in Appendix C. For given p, the S values are lower than previously found with BLASTPol for the Vela C molecular (Fissel et al. 2016) and with *Planck* for the Gould Belt clouds (Planck Collaboration XII 2018).

4.6.2. Polarisation fraction in SCUBA-2 observations

We calculated the bias-corrected polarisation fraction estimates p_{mas} from SCUBA-2 (I, Q, U) maps that were first convolved to a resolution of 40″ to increase their S/N. In Fig. 14 we plot p_{mas} as a function of column density for with $N(H_2) > 10^{22}$ cm^{-2}. We avoid a criterion based on the S/N of the polarised intensity because that would bias the selection of the polarisation fraction values. Based on Fig. 9, the plotted p_{mas} values should be unbiased. The average p_{mas} value decreases as a function of N and, based on the formal uncertainty of the weighted least squares fit, the decrease is significant.

The pixels associated with 70 μm sources (Fig. 14a) do not differ from the general distribution. However, at lower column densities (not shown), they tend to trace the lower envelope of the (N, p_{mas}) distribution. This is mostly a result of them having on average ~80% higher S/N (higher intensity for a given column density). This makes their p estimates less biased.

Appendix C shows further how the p_{mas} vs. N relation changes as a function of resolution and, consequently, as a function of the S/N. There we also present simulations of the p_{mas} vs. N relation in the presence of noise. These show that while the noise produces significant scatter, the average p_{mas} values estimated at the highest column densities are reliable.

The correlations between p_{mas}, S, and $N(H_2)$ and their dependence on the data resolution are further examined in Fig. 15. The values are independent of the resolution only towards the highest column densities. Otherwise, p_{mas} and S decrease with lower resolution. This is consistent with the increasing S/N reducing the bias and data below $N(H_2) \sim 10^{22}$ cm^{-2} remaining affected by noise. However, there may be additional effects from the averaging of observations with different polarisation angles (geometrical depolarisation). The S values may reflect the fact that the G035.39-00.33 field consists of a single, very narrow filament. For a given column density, a larger lag means that S calculation uses data over a larger area and thus on average with a lower S/N.

Figure 15d shows the correlation of S vs. p_{mas}. For column densities $N(H_2) > 2 \times 10^{22}$ cm^{-2}, with lower resolution

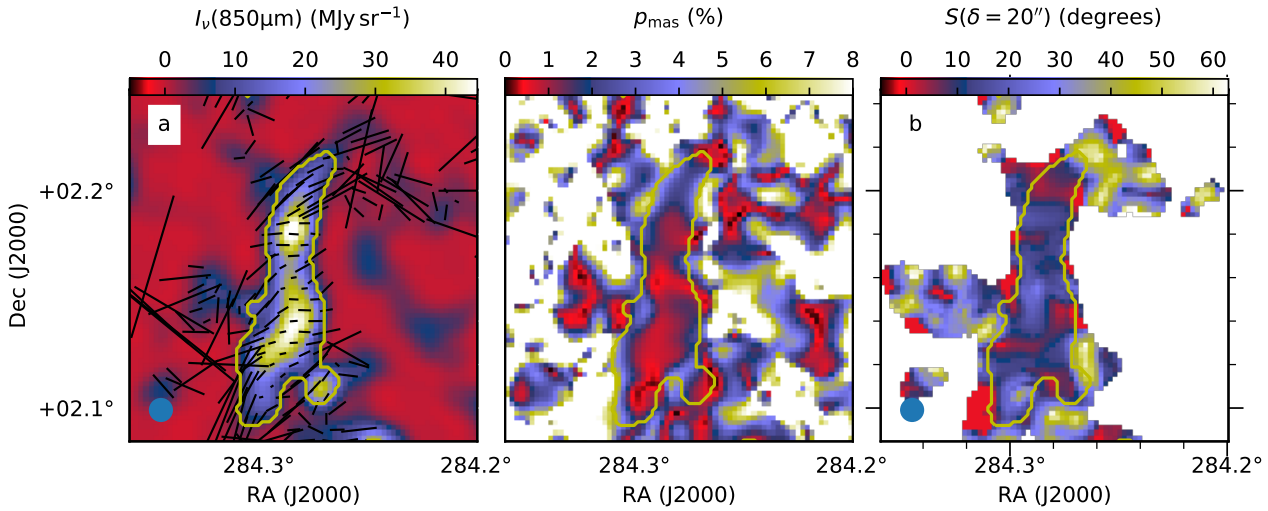

Fig. 11. Field orientation on the POL-2 850 μm intensity map (*panel a*), polarisation fraction $p_{\rm mas}$ (*panel b*), and polarisation angle dispersion function $S(\delta = 20'')$; *panel c*) calculated from data at 40″ resolution. Polarisation vectors (at 20″ steps, rotated to show the magnetic field orientation) and S are shown for pixels with $N(H_2) > 5 \times 10^{21}$ cm^{-2}. The length of the polarisation vectors per cm is the same as in Fig. 10 (14.4″ for a polarisation fraction of 1%). The yellow contours correspond to $N(H_2) = 10^{22}$ cm^{-2}, outside of which polarisation angles are uncertain.

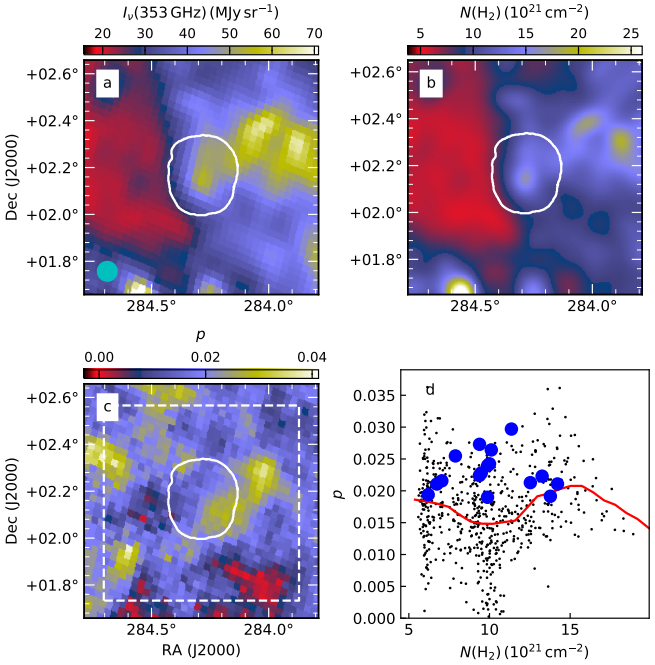

Fig. 12. Polarisation fraction of the G035.39-00.33 region based on *Planck* data. *Panel a* shows the 850 μm surface brightness, *panel b* the *Herschel* column density map convolved to 5′ resolution, and *panel c* a map of the polarisation fraction $p_{\rm mas}$ from *Planck* data. The white contour indicates the coverage of the SCUBA-2 map. *Panel d* shows the polarisation fraction as a function of column density, sampled with 2′ steps from maps at 5′ resolution, excluding the map boundaries (indicated by dashed lines in *panel c*), without a S/N cut-off. The red line is the running mean and the blue circles show values from the area covered by SCUBA-2 observations.

(higher S/N) the values converge towards similar parameter combinations as in Fig. 13 for *Planck*. This in spite of the fact that the *Planck* result is for a much larger area and for a data resolution lower by almost a factor of 4. Because of the small dynamical range (in part due to the spatial filtering) and possible residual bias in S, no clear anti-correlation is seen between the POL-2 estimates of p and S.

If the p–N anti-correlation were due to a loss of grain alignment, the product $p \times S$ should decrease as a function of increasing column density and decreasing dust temperature. Figure 15c shows the anti-correlation with the column density. In Fig. 16 we show the corresponding correlation of $p \times S$ with the dust colour temperature. Although the data selection (resolution of 40″ and column densities $N(H_2) > 2 \times 10^{22}$ cm^{-2}) should ensure that p values are unbiased, the polarisation angle dispersion function S may still contain some bias that contributes to increased $p \times S$ values at higher temperatures, which mainly correspond to lower column densities. The dispersion is calculated using data from an area with a diameter of $1.5 \times FWHM$. Therefore, high N at the central position does not fully preclude the S estimate being affected by lower S/N pixels further out. A Monte Carlo simulation based on the I, Q, and U maps and their error maps shows that the trend in Fig. 16 is not significant and thus neither proves or disproves the presence of grain alignment variations.

5. Radiative transfer models

5.1. Radiative transfer modelling of total emission

Figure 17 compares the column densities of two RT models fitted to SPIRE data. These differ regarding the assumed submillimetre vs. NIR opacity but have identical opacity at 250 μm. The model A has an opacity ratio of $\tau(250\,\mu{\rm m})/\tau({\rm J}) = 1.6 \times 10^{-3}$. This value is the average value derived for a sample of PGCC clumps in Juvela et al. (2015b) and a lower limit for the values estimated in Sect. 4.3. To test the sensitivity to dust properties, the alternative model B has $\tau(250\,\mu{\rm m})/\tau({\rm J}) = 1.0 \times 10^{-3}$. Model B results in 20% higher χ^2 values but both models represent the surface brightness data of the main filament equally well. The lower $\tau(250\,\mu{\rm m})/\tau({\rm J})$ ratio leads to higher column densities, with a 30% difference in the densest regions. The effect is thus of similar magnitude as the change in the assumed opacity ratio.

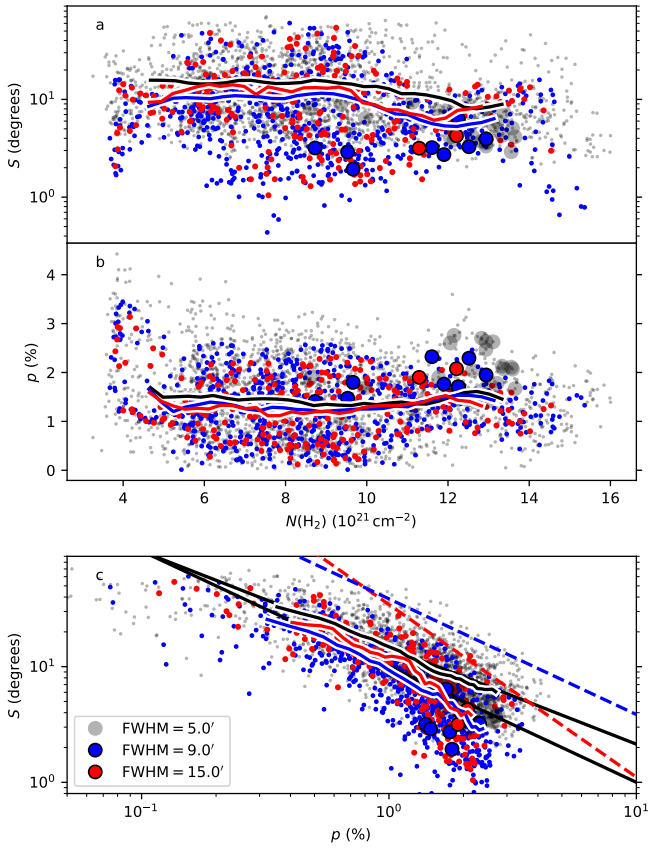

Fig. 13. Polarisation angle dispersion function S and polarisation fraction $p_{\rm mas}$ from *Planck* data in a $2^\circ \times 2^\circ$ area centred on the POL-2 field. *Panels a and b* show these as a function of dust optical depth and *panel c* shows their mutual correlation. The colours of the plot symbols correspond to the data resolution, as indicated in *panel c*. The solid lines show the corresponding moving averages. The points inside the area mapped with POL-2 are plotted with large symbols. The data are sampled at steps of $FWHM/2$ and S is calculated for lag $\delta = FWHM/2$. In *panel c* the upper solid black line shows the relation $\log_{10}(S) = -0.834 \times \log_{10}(p_{\rm mas}) - 0.504$ from Planck Collaboration Int. XIX (2015) and the lower black line the relation $S = 0.1/p_{\rm mas}$. The red dashed line is the relation $\log p_{\rm mas} = -0.670 \log S - 0.97$ from Fissel et al. (2016). The blue dashed line corresponds to the fit to Gould Belt cloud data, $S \times p = 0.31^\circ (FWHM/160')^{0.18}$ of Planck Collaboration XII (2018), calculated with $FWHM = 9'$.

Figure 17 also shows $N(\rm H_2)$ estimates that were calculated using MBB fits and the simulated surface brightness maps of the model A. As expected, the values recovered with MBB calculations are below the true values. The difference becomes noticeable above $N(\rm H_2) = 2 \times 10^{22}$ cm^{-2} and at $N(\rm H_2) = 10^{23}$ cm^{-2} the error is a factor of 2.

5.2. Radiative transfer modelling of the p vs. N relation

We added to model *A* (see Sect. 5.1) alternative descriptions of the magnetic field geometry to make predictions of the polarised emission. These calculations are used to test how the field geometry could affect the observed polarisation patterns and especially the variations of the polarisation fraction as a function of the column density. A physical cloud model is needed to describe the variations of the dust emission that depend on the temperature structure of the cloud. In RAT grain alignment calculations, the volume density and the variations of the radiation field (intensity and anisotropy) become additional factors.

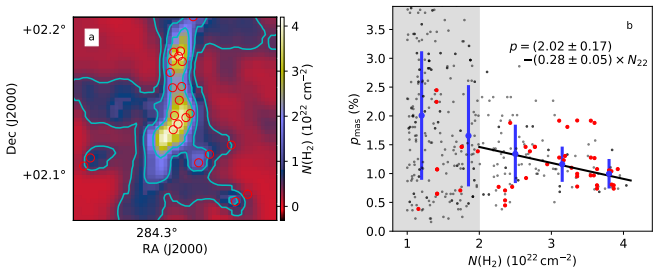

Fig. 14. POL-2 polarisation fraction and column density. *Panel a* shows the column density map $N_5(\rm H_2)$ at $40''$ resolution. The contours are drawn at 0.5, 1, and 2 times 10^{22} cm^{-2} and the red circles denote the locations of the point sources of Table 2. In *panel b*, $p_{\rm mas}$ is plotted as a function of column density for data with $N(\rm H_2) > 10^{22}$ cm^{-2}. The pixels coinciding with point sources (red circles of panel a) are plotted in red. The blue bars are representative error estimates. The result of the weighted least squares fit to data at $N(\rm H_2) > 2 \times 10^{22}$ cm^{-2} is given in the panel and is shown as a black solid line. The shading corresponds to $N(\rm H_2) < 2 \times 10^{22}$ cm^{-2} where the $p_{\rm mas}$ estimates may be biased.

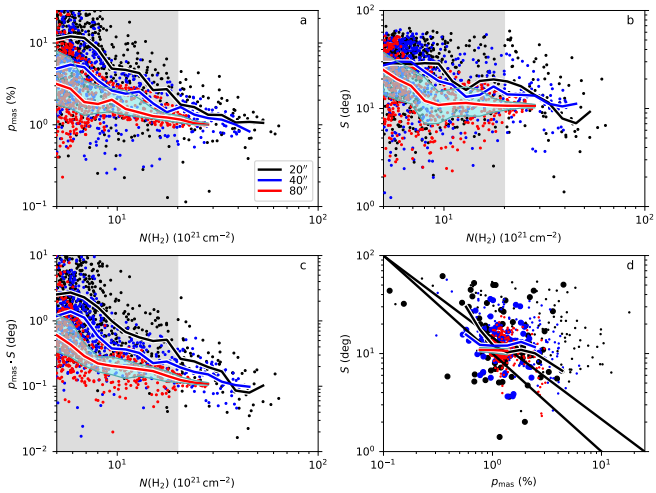

Fig. 15. Correlations between POL-2 polarisation parameters $p_{\rm mas}$ and S and the column density. The quantities are calculated at four spatial resolutions represented with the colours indicated in *panel a*. The data are sampled at steps of $FWHM/2$ and the solid lines correspond to running averages. In *panels a–d*, the shading corresponds to $N(\rm H_2) < 2 \times 10^{22}$ cm^{-2} where, according to Fig. 9, the $40''$ resolution $p_{\rm mas}$ estimates become unreliable. In *panel d*, values for 10^{22} cm$^{-2} < N(\rm H_2) < 2 \times 10^{22}$ cm^{-2} and $N(\rm H_2) > 2 \times 10^{22}$ cm^{-2} are shown with small and large symbols, respectively, and the lines show running averages for the higher column density interval (20 logarithmic bins over the parameter range with a minimum of four points per bin). Shaded cyan region corresponds to the interquartile range of the quantities plotted with red lines. In *panel d* the upper solid black line shows the relation $\log_{10}(S) = -0.834 \times \log_{10}(p_{\rm mas}) - 0.504$ from Planck Collaboration Int. XIX (2015) and the lower black line the relation $S = 0.1/p_{\rm mas}$.

Because the simulations are essentially free of noise, p values can be estimated directly without using the $p_{\rm mas}$ estimator.

We used cloud models that were optimised for the $\tau(250\ \mu{\rm m})/\tau({\rm J}) = 1.6 \times 10^{-3}$ dust. We started with a model where the main volume is threaded by a uniform magnetic field in the plane of the sky and with a position angle PA = 45°, in rough correspondence to the *Planck* data in Fig. 10. At densities above $n(\rm H_2) = 3 \times 10^3$ cm^{-3}, the field is in EW direction (PA = 95°) except for the northern part Dec > 2°10′ where it has PA = 135° and thus is perpendicular to the large-scale field.

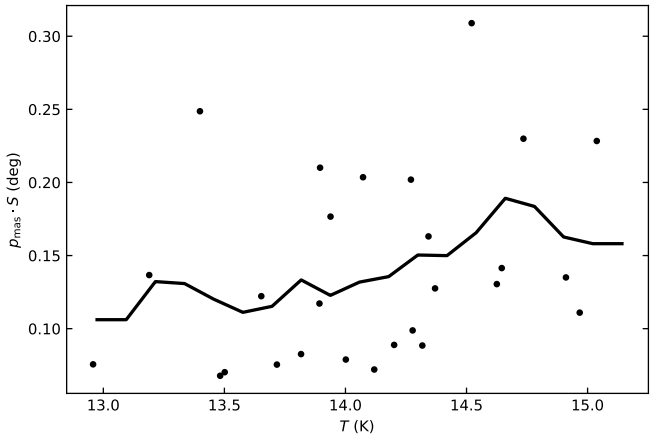

Fig. 16. Product $p \times S$ as a function of dust colour temperature. The data are at 40″ resolution, sampled at half-beam steps, and selected from the region with $N(H_2) > 2 \times 10^{22}$ cm^{-2}. The solid line shows a moving average.

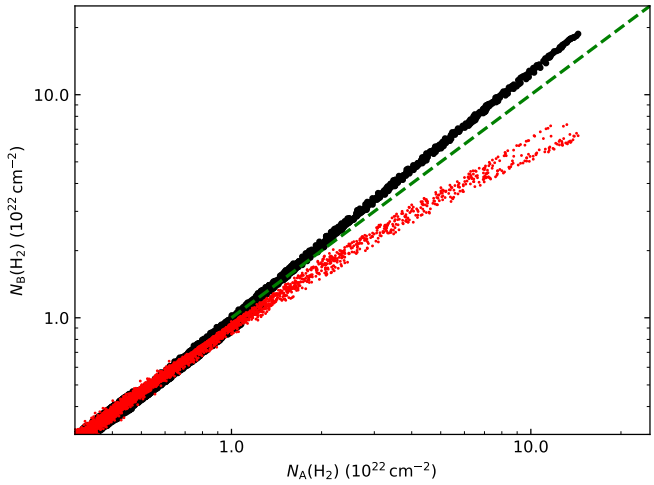

Fig. 17. Correlation between the column densities $N(H_2)$ of two RT models fitted to observations. Column densities N_A and N_B (black dots) correspond to dust models with $\tau(250\ \mu m)/\tau(J)$ equal to 1.6×10^{-3} and 1.0×10^{-3}, respectively. For the RT model with column densities N_A, the red points show the column density estimates derived from the synthetic surface brightness maps. The dashed line is the one-to-one relation. All data are at 20″ resolution.

The results for spatially constant grain alignment and for calculations with RAT alignment are shown in Figs. 18 and 19, respectively. The POL-2 simulation again assumes that the measured (I, Q, U) are high-pass filtered at a scale of $\theta = 200''$. The absolute level of p is scaled to give a maximum value of 5% for the synthetic *Planck* observations and the same scaling is applied to the POL-2 case.

In Fig. 18 the simulated *Planck* observations show some 30% decrease in p as a function of column density. Because the grain alignment was uniform, the drop is caused by changes in the magnetic field orientation. In the simulated POL-2 observations, the orientation of the polarisation vectors follows the magnetic field of the dense medium. Unlike in the actual observations, the polarisation fraction is close to the $p = 5\%$ level, the same as for *Planck*. The polarisation fraction of the northern clump is only slightly lower, some 4%. This is a result of the lower density (and smaller size) of that clump and of the magnetic field orientation that is perpendicular to the large-scale field.

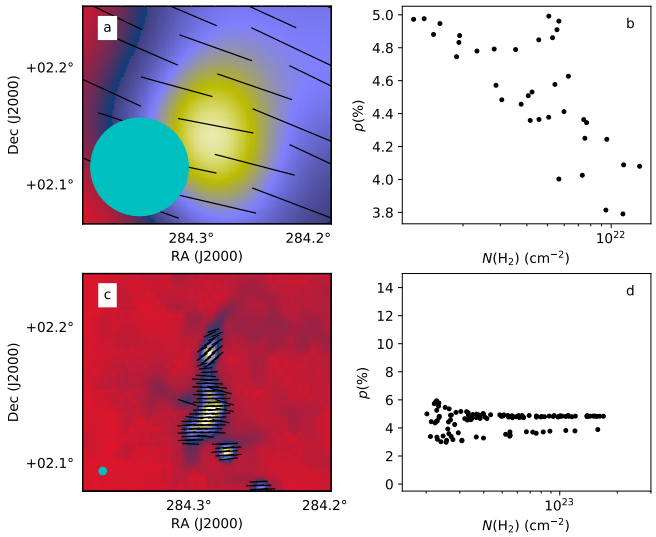

Fig. 18. Predictions of the toy magnetic field model with constant grain alignment. The polarisation vectors are shown on the column density map in *panel a* (central part of the full map) and the p vs. $N(H_2)$ relation is plotted in *panel b* at *Planck* resolution. The *lower panels* are the same for synthetic POL-2 observations, at a resolution of 20″, assuming high-pass filtering with $\theta = 200''$. The scaling of the absolute p values is arbitrary but identical between the panels.

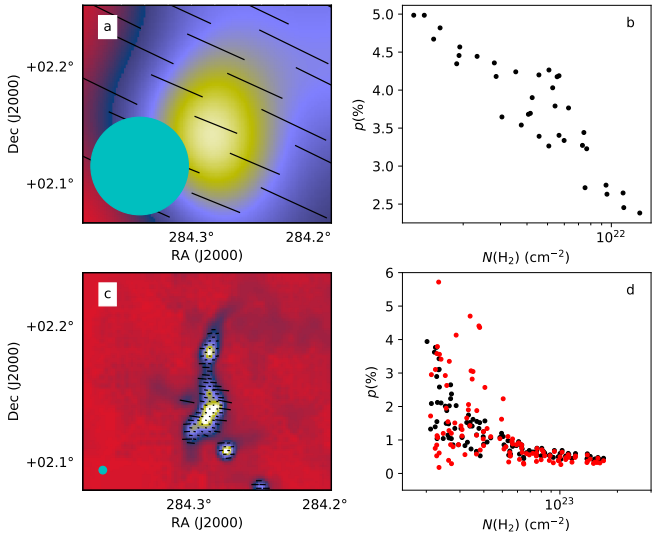

Fig. 19. Same as Fig. 18, but using grain alignment predicted by RAT calculations. In *panel d*, the red points correspond to data with spatial high-pass filtering with a scale of $\theta = 100''$ instead of the default value of $\theta = 200''$.

Appendix D shows results when the change from the large-scale field takes place at a higher density, $n(H_2) = 10^4$ cm^{-3} instead of $n(H_2) = 3 \times 10^3$ cm^{-3}. This has only a very small effect on the polarisation fraction, except for the northern clump where p drops partly below 2%.

When the alignment predicted by RAT is taken into account (Fig. 19), the POL-2 polarisation fractions drop below the *Planck* values but now the *Planck* values show an even slightly stronger dependence on column density, in contrast with the observations of the G035.39-00.33 field. Figure 19d shows p vs. $N(H_2)$ also for a POL-2 simulation where the data are assumed to be high-pass filtered at a scale of $\theta = 100''$ instead of $\theta = 200''$. The different filtering does not have a strong

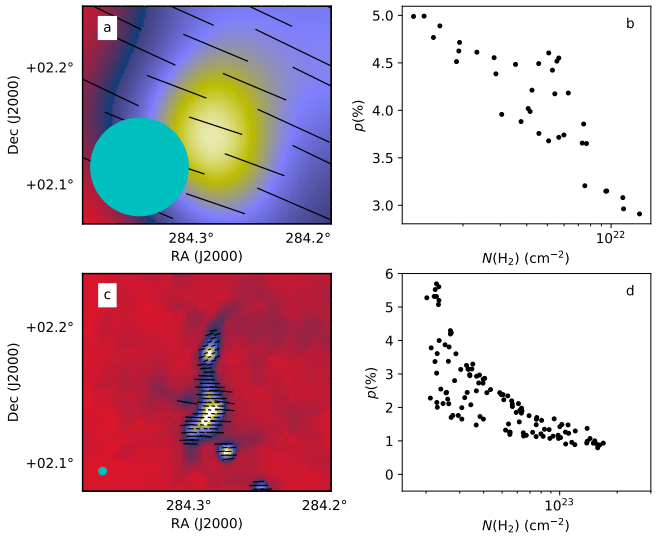

Fig. 20. Same model with RAT alignment as in Fig. 19, but assuming a factor of 2 larger grain sizes.

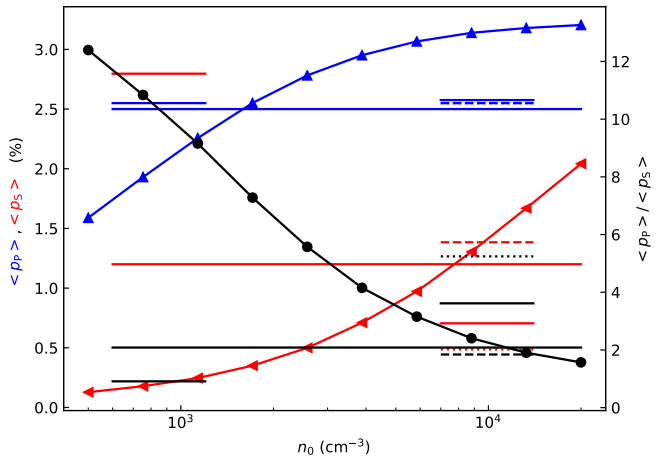

Fig. 21. Polarisation fractions for different grain alignment models. The long horizontal lines show the observed average values of p (left y-axis) for the *Planck* (p_P, blue line) and the POL-2 (p_S, red line) observations. The black long horizontal line stands for the observed $\langle p_\mathrm{P}\rangle/\langle p_\mathrm{S}\rangle$ ratio (right y-axis). The three curves with markers show the corresponding quantities for models that assume a loss of grain alignment above the density threshold n_0. The results for models with constant grain alignment are indicated with short horizontal lines near $n = 10^3$ cm^{-3}. The RAT models are shown as short horizontal lines near $n = 10^4$ cm^{-3}, for the default model (solid lines), for the case with larger grain sizes (dashed line), and for an alternative model with a smaller $\tau(250\,\mu\mathrm{m})/\tau(\mathrm{J})$ ratio (dotted line).

effect but leads to some larger values towards the edges of the filament.

The RAT calculations of Fig. 19 were not completely self-consistent because they employed the original grain size distributions (see Sect. 3.3) while assuming an increased dust opacity at sub-millimetre wavelengths. We made an alternative simulation where the grain alignment (and thus the polarisation reduction factor) was calculated assuming a factor of 2 larger grains. The comparison of these results in Fig. 20 with the previous calculations of Fig. 19 should partly quantify the uncertainty associated with the particle sizes. A factor of 2 change in the grain size in first approximation corresponds to a factor of two increase in the POL-2 polarisation fractions. The effect on the simulated *Planck* observations is small, because most grains were already aligned outside the dense filament. For RAT alignment with the larger grain sizes, Appendix D shows results for an alternative model where the POS magnetic field orientations are taken from POL-2 observations (at 20″ resolution) for the model volume with $n(\mathrm{H_2}) > 3\times10^3$ cm^{-3}. There the polarisation fractions are on average lower only by a fraction of a percent. The difference is larger in the northern clump, which is sensitive to changes in the magnetic field configuration, probably because of the stronger geometrical depolarisation that results from the orthogonality of the local and the extended fields.

Figure 21 compares the constant alignment and RAT cases with models where R has an ad hoc dependence on the volume density. The grains are perfectly aligned at low densities but R decreases smoothly to zero above a density threshold n_0,

$$R = 0.5 + 0.5\tanh\left[\log_{10}(n_0) - \log_{10}(n)\right]. \quad (15)$$

In the modelling, the absolute scale of p is left free. In Fig. 21 the values are scaled so that the *Planck* polarisation fraction is 2.5% or have a maximum value of 3% in the case of the n_0 dependence. The only real constraint is provided by the ratio of the *Planck* and POL-2 polarisation fractions. The observed ratio ~2.5 is reached for a density threshold of $n_0 = 10^4$ cm^{-3}. The constant-alignment model predicts a smaller ratio while the initial RAT model gives a higher ratio. However, if RAT calculation assume a factor of 2 larger grain sizes, the ratio falls slightly below the observed value.

Finally, we also examined models where the dust opacity ratio was $\tau(250\ \mu\mathrm{m})/\tau(\mathrm{J}) = 1.0\times10^{-3}$. The lower sub-millimetre opacity means that the modelling of surface brightness data led to larger volume densities and to a lower radiation field intensity inside the cloud. Both factors contribute to a lower grain alignment in RAT calculations (see Eq. (14)). In Fig. 21 the change from $\tau(250\,\mu\mathrm{m})/\tau(\mathrm{J}) = 1.6\times10^{-3}$ to $\tau(250\,\mu\mathrm{m})/\tau(\mathrm{J}) = 1.0\times10^{-3}$ increases the ratio of *Planck* and POL-2 polarisation fractions by over 30%.

Unfortunately, the observed p ratio does not provide strong constraints on the grain alignment because the quantitative results also depend on the assumed magnetic field geometry. As an example, we tested a field configuration where the southern filament has a toroidal field at densities above $n = 3\times10^3$ cm^{-3} while the field in the northern part is still uniform (poloidal). A toroidal field is consistent with the observed magnetic field orientation that is perpendicular to the southern filament. Regarding the p vs. N relation, it is also an interesting special case that results in stronger geometrical depolarisation as one moves away from the symmetry axis. The results for the constant alignment and an RAT alignment models are shown in Figs. 22 and 23. In the constant alignment case the *Planck* polarisation fractions have not changed but the POL-2 values show a larger scatter and a lower average polarisation fraction. At the borders of the filament, where the toroidal field is along the LOS in the dense medium, the polarisation vectors have turned parallel to the large-scale field. The change is qualitatively similar for the RAT case (Fig. 23). The p vs. N relation is flatter than in Fig. 19 but not significantly different from the observations shown in Fig. 14b. In the model the toroidal configuration also causes a stronger drop in the *Planck*-observed polarisation fraction. A more extended toroidal component (e.g. in a test where the density threshold was reduced from $n = 3\times10^3$ cm^{-3} to $n = 5\times10^2$ cm^{-3}) would cause clear changes also in the orientation of the *Planck*-detected polarisation vectors. However, these

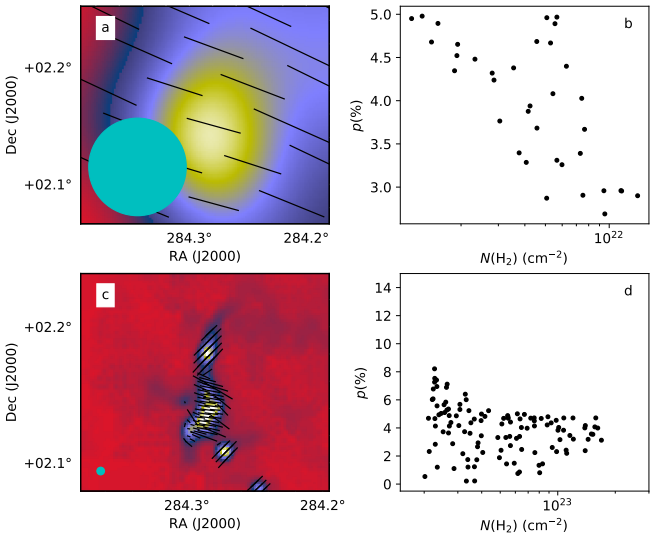

Fig. 22. Same as the constant alignment case of Fig. 18 but assuming a toroidal field for the southern clump.

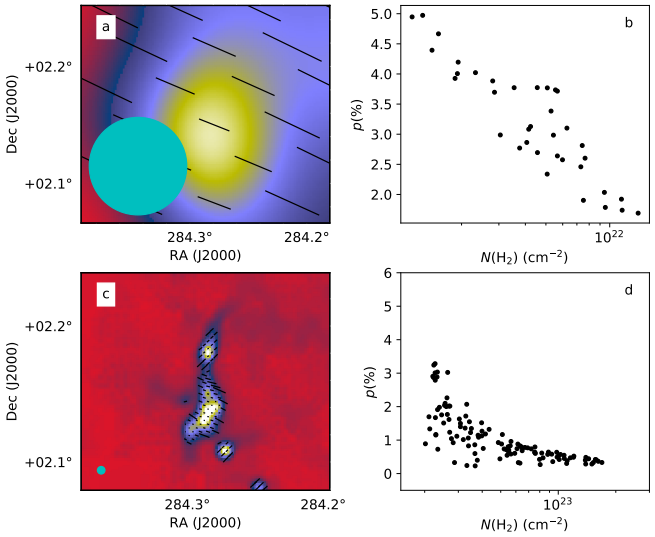

Fig. 23. Same as the RAT alignment case of Fig. 19 but assuming a toroidal field for the southern clump.

effects are dependent on our assumptions of the LOS matter distribution and would disappear if most of the extended material was located far from the filament.

6. Discussion

In the following, we discuss the results regarding the observable dust properties (Sect. 6.1) and the polarisation fraction (Sect. 6.2).

6.1. Dust opacity in the G035.39-00.33 field

The G035.39-00.33 field has a high-column-density background of $N(\mathrm{H_2}) \sim 10^{22}\,\mathrm{cm^{-2}}$ (Fig. 3). Even after the subtraction of this background, the column densities are above $N(\mathrm{H_2}) = 2 \times 10^{22}\,\mathrm{cm^{-2}}$ over a filament length of ∼7′ (∼6 pc). With a typical filament width of ∼40″, the average volume density is of the order of $n(\mathrm{H_2}) \sim 10^4\,\mathrm{cm^{-3}}$. With the high volume density and the dust temperatures below 14 K (with minima close to $T = 12$ K, see Sects. 4.1 and 4.2), the conditions are suitable for grain evolution. The properties of dust opacity can thus be expected to be different from those of diffuse clouds.

The comparison of dust sub-millimetre emission and NIR/MIR observations gave an average opacity ratio of $\tau(250\ \mu\mathrm{m})/\tau(\mathrm{J}) = (2.55 \pm 0.03) \times 10^{-3}$, which also is close to the behaviour of the southern clump. The relation is steeper in the northern clump, although only in small ∼1′ region that is close to some 70 μm sources. Internal heating could reduce the degree to which dust optical depth $\tau(250\ \mu\mathrm{m})$ is underestimated. The fit at $\tau(\mathrm{J}) < 6$ gave a lower value of $\tau(250\ \mu\mathrm{m})/\tau(\mathrm{J}) = (1.72 \pm 0.04) \times 10^{-3}$. In the RT models, $\tau(\mathrm{J}) \sim 6$ ($\tau(250\,\mu\mathrm{m}) \sim 0.012$ typically corresponds to a LOS peak volume density of the order of $n(\mathrm{H_2}) = 5 \times 10^3\,\mathrm{cm^{-3}}$. Planck studies have found in diffuse regions values $\tau(250\,\mu\mathrm{m})/N(\mathrm{H}) \sim 0.55 \times 10^{-25}\,\mathrm{cm^2\,H^{-1}}$ (Planck Collaboration XI 2014; Planck Collaboration Int. XVII 2014). With the Bohlin et al. (1978) relation between the reddening and hydrogen column density and with the $R_\mathrm{V} = 3.1$ extinction curve (Cardelli et al. 1989), this corresponds to $\tau(250\ \mu\mathrm{m})/\tau(\mathrm{J}) = 0.41 \times 10^{-3}$. The G035.39-00.33 sub-millimetre opacity values relative to NIR are thus more than four times higher than in diffuse clouds.

The correlation between density and sub-millimetre opacity is known from numerous studies (Kramer et al. 2003; Stepnik et al. 2003; Lehtinen et al. 2004; del Burgo & Laureijs 2005; Ridderstad & Juvela 2010; Bernard et al. 2010; Martin et al. 2012; Suutarinen et al. 2013; Ysard et al. 2013; Roy et al. 2013; Svoboda et al. 2016; Webb et al. 2017). Juvela et al. (2015b) used *Herschel* observations to study sources from the Planck Catalogue of Galactic Cold Clumps (PGCC; Planck Collaboration XXVIII 2016). For a sample of 23 fields, the average dust opacity was $\tau(250\ \mu\mathrm{m})/\tau(\mathrm{J}) = 1.6 \times 10^{-3}$. Given that this value corresponds to sources with optical depths below $\tau(\mathrm{J}) \sim 3$, it is in qualitative agreement with the results of the present study. In Juvela et al. (2015b), the maximum values derived for individual clumps were $\tau(250\ \mu\mathrm{m})/\tau(\mathrm{J}) = 4 \times 10^{-3}$, similar to the value of the northern clump of G035.39-00.33. However, in that study the NIR extinction estimates were based on background stars only and, in the case of high optical depths, have a higher uncertainty.

A large $\tau(250\ \mu\mathrm{m})/\tau(\mathrm{J})$ ratio also could result from an underestimation of the $\tau(\mathrm{J})$ values in the G035.39-00.33 field. The lack of background stars should not directly affect the $\tau(\mathrm{J})$ estimates of the densest filament, which are based more on MIR data but if the MIR emission had a strong foreground component, that could also lead to low $\tau(\mathrm{J})$ estimates. The uncertainty of extinction depends non-linearly on the foreground intensity but it is probably only some 10–20% (see also Butler & Tan 2012b). In the analysis of Kainulainen & Tan (2013), the MIR extinction also was tied to the NIR extinction measurements, which makes large errors in the extinction levels improbable. Even with an uncertainty of 30% (see Kainulainen & Tan 2013), the 1-σ lower limit is still above the average value of Juvela et al. (2015b).

The estimates of the sub-millimetre opacity $\tau(250\ \mu\mathrm{m})$ are likely to be biased because they were derived from single-temperature MBB fits, ignoring the effects of LOS temperature variations. Figure 17 compared the true column densities of a model cloud to those derived from the synthetic surface brightness maps. This also serves as an estimate for the bias of the $\tau(250\ \mu\mathrm{m})$ values. At a column density of $N(\mathrm{H_2}) = 10^{23}\,\mathrm{cm^{-2}}$ the estimated bias is more than a factor of 2. This column density is higher than the values $N(\mathrm{H_2}) \lesssim 5 \times 10^{22}\,\mathrm{cm^{-2}}$ estimated for G035.39-00.33. However, these are consistent if the latter are underestimated by the factor indicated by the modelling.

Quantitatively, the bias predictions depend on how well the models represent the real cloud. A stronger internal heating would decrease the bias, at least locally. Conversely, the observations do not give strong constraints on the maximum (column) densities and higher optical depths would lead to a higher bias. The relative bias is likely to be at least as large in $\tau(250\ \mu\mathrm{m})$ as in $\tau(\mathrm{J})$. Thus, the true value of $\tau(250\ \mu\mathrm{m})/\tau(\mathrm{J})$ may be even higher than the quoted estimate of 2.55×10^{-3}.

The calculation of the sub-millimetre opacity assumed a fixed dust opacity spectral index of $\beta = 1.8$, which is close to the spectral index estimated from the data (see below). An error of ~0.1 in the spectral index would correspond only to ~10% error in opacity. For further discussion of the effect of the spectral index and the extinction law, see Juvela et al. (2015b). Finally, if the actual resolution of our $\tau_5(250\,\mu\mathrm{m})$ map were lower than the nominal 15″, this would lower the $\tau(250\ \mu\mathrm{m})/\tau(\mathrm{J})$ estimates. When the maps were convolved to a lower resolution with a Gaussian beam with $FWHM = 20''$, the opacity ratio changed by less than 0.03 units. This shows that the result is not sensitive to the resolution.

We estimated a dust opacity spectral index of $\beta \sim 1.9$ for the main G035.39-00.33 filament, using data at $\lambda \leq 850\,\mu$m. For the northern part separately, the β values were slightly lower but there both the SCUBA-2 450 μm and 850 μm values were above the relation fitted to SPIRE data (Fig. 5). These offsets and thus the lower β values could be caused by uncertainties in the spatial filtering or, when using background-subtracted data, the reference region being located at a larger distance in the south (see Fig. 1b).

The derived β value is practically identical to the median value $\beta = 1.91$ that Juvela et al. (2015a) reported for a sample of GCC clumps based on *Herschel* data with $\lambda \leq 500\,\mu$m. In Juvela et al. (2015b), the inclusion of longer wavelength *Planck* data resulted in a smaller value of $\beta = 1.66$. This wavelength dependence had been demonstrated, for example, in Planck Collaboration Int. XIV (2014). More recently, Juvela et al. (2018) analysed *Herschel* and SCUBA-2 observations of cores and clumps within some 90 PGCC fields. For those objects the median value at *Herschel* wavelengths was $\beta \sim 1.8$ (although with significant scatter) and the inclusion of the SCUBA-2 850 μm data point decreased the value closer to $\beta \sim 1.6$. The higher spectral index value of the G035.39-00.33 field is again in qualitative agreement with G035.39-00.33 being more dense and, in terms of dust evolution, probably a more evolved region. Spectral indices are generally observed to be higher towards the end of the prestellar phase while in the protostellar phase one may again observe lower values (Chen et al. 2016b; Li et al. 2017; Bracco et al. 2017). This may be caused by dust evolution (e.g. further grain growth), by the temperature variations resulting from internal heating, or directly by problems associated with the analysis of observations at very high column densities (Shetty et al. 2009b,a; Malinen et al. 2011; Juvela & Ysard 2012a,b; Ysard et al. 2012; Juvela et al. 2013b; Pagani et al. 2015). The G035.39-00.33 field does contain a number of protostellar objects, but in this paper we only examined the average β over the whole filament.

6.2. Polarisation

The polarisation observations trace a combination of magnetic field morphology and grain properties. *Planck* and POL-2 provided different views into the structure of the magnetic fields. The large-scale field was found to be uniform while the small-scale structure associated with the dense filament was more varied, even with partly orthogonal orientations. The *Planck* and POL-2 data are not contradictory because of the large difference in the beam sizes. POL-2 also is not sensitive to the extended emission (Sect. 4.5). Nevertheless, the change in the field orientations must be constrained to a narrow region at and around the main filament. Otherwise, these would be visible also in *Planck* data, as deviations from the average field orientation and as a reduced net polarisation. If connected to the gravitational instability of the filament and of the embedded cores, the effects are naturally confined in space. If strong accretion flows extend to a distance of ~1 pc, this corresponds to only ~1′ in angular distance.

In the following, we discuss in more detail the observations and the modelling of the polarisation fraction.

6.2.1. Observed polarisation fractions

The polarisation fraction p is generally observed to decrease towards dense clouds and especially towards dense (prestellar) clumps and cores (Vrba et al. 1976; Gerakines et al. 1995; Ward-Thompson et al. 2000; Alves et al. 2014; Planck Collaboration Int. XX 2015; Planck Collaboration Int. XXXIII 2016).

The *Planck* data were used to characterise the large-scale environment of the G035.39-00.33 filament. *Planck* data did not show any clear column density dependence over the examined $2^\circ \times 2^\circ$ area and the bias-corrected polarisation fraction estimate p_{mas} remained within a narrow range between 1 and 3% (Fig. 12). The same was already evident based on the polarisation vectors that were plotted in Fig. 10a. These show that the large-scale magnetic field orientation is very uniform, also in the area covered by POL-2 observations. The dynamical range of column density over this area was only a factor of ~3, which partly explains the lack of a clear correlation. The polarised signal is largely dominated by extended emission not directly connected to the dense filament. Because of the low Galactic latitude, there can be contributions from many regions along the LOS, which would tend to decrease the observed polarisation fraction (Jones et al. 1992; Planck Collaboration Int. XIX 2015). In Liu et al. (2018b), multiple velocity components were identified from ^{13}CO and C^{18}O line data. Only the 45 km s^{-1} feature, the strongest of the kinematic components, is associated with the main filament. This is consistent with the picture shown by Figs. 1a and 3. At *Herschel* resolution the filament rises more than a factor of 4 above the extended column density background while at the *Planck* resolution it is associated with a mere 50% increase above the background surface brightness. With the added effect of spatial filtering, POL-2 measurements are only sensitive to the emission from the main filament. Conversely, *Planck* measurement could be slightly affected by the dense filament, unless that is associated with lower polarisation fractions.

The uniformity of the magnetic field is shown quantitatively by the polarisation angle dispersion function S calculated from the *Planck* data. Figure 13c showed the relation $\log p = -0.670 \log S - 0.97$ that Fissel et al. (2016) derived from BLASTPol observations of the Vela C molecular cloud (ISRF-heated sightlines). Compared to this, the *Planck* data of the G035.39-00.33 field indicate much lower (p, S) parameter combinations. Figure 13c also included the relation $\log_{10}(S) = -0.834 \times \log_{10}(p_{\mathrm{mas}}) - 0.504$ that Planck Collaboration Int. XIX (2015) obtained at larger scales ($FWHM = 1^\circ$, $\delta = 30'$), using data over a large fraction of the whole sky. This relation corresponds to higher values of

S and p than found in the G035.39-00.33 field. The comparison to the *Planck* results (Planck Collaboration Int. XIX 2015) is not straight forward because observations probe different linear scales ($FWHM = 1^\circ$ compared to $FWHM = 9 - 15'$ in our analysis). Figure 13 did not show a systematic dependence on the scale. Planck Collaboration XII (2018) detected a shallow relation of $S \times p \propto FWHM^{0.18}$, which would thus be detectable only by using a wider range of scales. According to that relation, the $S \times p$ values at $15'$ resolution should be only some 22% smaller than at 1° resolution.

Instead of grain alignment or the statistical averaging of LOS emission with different polarisation angles), lower G035.39-00.33 polarisation fractions (in relation to S) could be explained by a larger LOS component of the magnetic field, a hypothesis that we cannot directly test. Large angles between the magnetic field and the POS would tend to be associated with large values of S (Chen et al. 2016a). However, this is only a statistical correlation and cannot be used to exclude the possibility of a large LOS field component, which also would be consistent with the Galactic longitude and distance of the G035.39-00.33 field.

Compared to the low-resolution *Planck* data, the POL-2 data are more affected by observational noise. The bias-corrected polarisation fraction estimates $p_{\rm mas}$ are reliable for the central filament and are there $p_{\rm mas} \sim 1\%$ irrespective of the data resolution between $FWHM = 15''$ and $FWHM = 60''$ (see Fig. C.2).

The POL-2 $p_{\rm mas}$ estimates should be unbiased when used at $40''$ resolution and when the analysis is restricted to column densities $N(H_2) > 2 \times 10^{22}$ cm^{-2}. In this range, the decrease of polarisation fraction as a function of column density is significant (Fig. 14). The drop from $N(H_2) = 2 \times 10^{22}$ cm^{-2} to $N(H_2) = 4 \times 10^{22}$ cm^{-2} is from 1.5% to values below 1%. Because low-density regions along the LOS (in front of and behind the filament but possibly associated to it) will produce some polarised intensity, a non-zero polarisation fraction does not exclude the possibility of a complete loss of grain alignment within the densest filament.

The simulations presented in Appendix C confirm that the negative correlation between $p_{\rm mas}$ and $N(H_2)$ is larger than expected based on the noise alone (Fig. C.4). These also show that with column densities $N(H_2) > 10^{22}$ cm^{-2} and with $FWHM > 20''$, most of the resolution dependence of p can be attributed to geometrical depolarisation (Fig. C.5). This is related to the S function. *Planck* data showed some anti-correlation between $p_{\rm mas}$ and S (Fig. 8) but this dependence was not clear in POL-2 data. While Fig. 11 gave some indications, especially in the northern part, statistically the anti-correlation remained weak (Fig. 15d). Reliable mapping of S would require higher S/N further out from the central filament. On the other hand, S also is also affected by the filtering of the extended emission.

Because polarisation fraction is correlated with column density, it could be expected to be correlated with tracers of dust evolution such as $\tau(250\ \mu{\rm m})/\tau({\rm J})$. However, physically high volume density should be associated with grain growth, which in turn works against drop of polarisation that in the RAT scenario is caused by the weakening of the radiation field. Figure 24 shows no clear correlation between $p_{\rm mas}$ and the opacity ratio $\tau(250\ \mu{\rm m})/\tau({\rm J})$ and only the correlation between $\tau(250\ \mu{\rm m})/\tau({\rm J})$ and $N(H_2)$ is significant (correlation coefficient $r = 0.45$, significant at ~98% level when calculated with data sampled at FWHM steps). As mentioned in Sect. 4.6.2, 70 μm sources tend to have lower than average polarisation fractions, in this sample 1.1 vs. 1.4%. Part of this is caused by their higher S/N and thus lower bias, although for the data in Fig. 24 the bias should not be very significant.

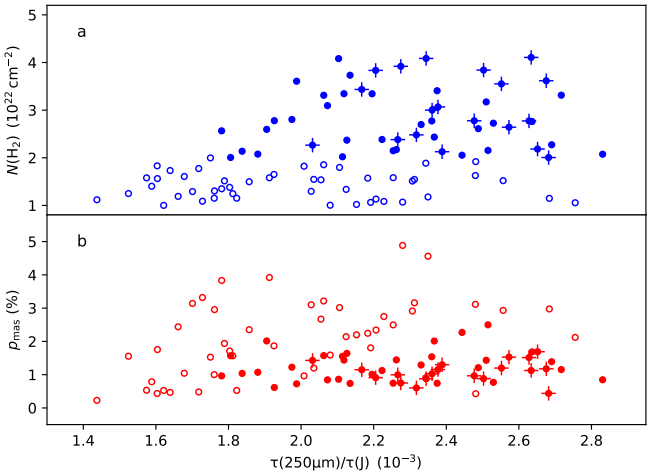

Fig. 24. Correlations between opacity ratio $\tau(250\ \mu)/\tau({\rm J})$ and column density (*panel a*) or POL-2 polarisation fraction (*panel b*). The data are at $40''$ resolution and sampled at half-beam steps. The points coinciding with the point sources marked in Fig. 14 are marked with plus signs. Data for column densities $N(H_2) < 2 \times 10^{22}$ cm^{-2} are plotted with open symbols and for these the $p_{\rm mas}$ estimates may be inaccurate.

6.2.2. Simulations of polarised emission

We used RT simulations to probe the effects that magnetic field geometry and grain alignment variations can have on the polarisation observations. Because the absolute values of the polarised intensity depend on poorly known grain properties, small-scale magnetic field structure, and the strength of the LOS magnetic field component, we concentrated on the ratio of the simulated *Planck* and POL-2 polarisation fractions.

In the case of constant grain alignment, the polarisation fractions were even higher in the simulated POL-2 data than in the simulated *Planck* data (Fig 18), in clear contradiction with observations. When grain alignment was assumed to depend on volume density, the ratio of *Planck* and POL-2 polarisation fractions could be matched with a density threshold of $n(H_2) = 10^4$ cm^{-3}. This can be compared to Alves et al. (2014; see also Alves et al. 2015), who analysed optical, NIR, and sub-millimetre observations of a starless core in the Pipe nebula. They deduced a loss of alignment at densities $n(H_2) > 6 \times 10^4$ cm^{-3}. The analyses are of course affected by many uncertainties (see Sect. 6.2.3) and, because of the larger distance, the linear resolution of our observations is much lower. If the difference in the density thresholds were significant, it could be related to the different nature of the sources (e.g. evolutionary stage and internal heating).

The low p values of the actual G035.39-00.33 observations could be explained by geometrical depolarisation resulting from line tangling within the densest filament. However, this does not seem a likely explanation given the local uniformity of the polarisation angles and the relatively constant polarisation fraction observed over the whole filament. The synthetic *Planck* p values also dropped by ~30% as a function of column density (Fig. 18b), while in the actual observations no clear column-density dependence was seen (Fig. 12c). However, our models described only a $13' \times 13'$ area and a volume of ~(11 pc)^3. About half of the actual *Planck* signal is coming from a more extended cloud component (cf. Figs. 1a and b) that appears to be associated with at least a factor of 2 higher polarisation fractions than the main filament. If the extended component was added, the p values would not change at low column densities while

the values towards the filament would increase significantly. Therefore, the p vs. N relation of the simulated *Planck* observations is not necessarily incompatible with the observations. A more remote possibility for such p vs. N relations would be to assume that the direction of the large-scale field is changing so that (unlike in simulations) it has a larger LOS component in the low-column-density regions (cf. Planck Collaboration Int. XXXIII 2016).

Figure 19 showed the results for a model where the grain alignment efficiency varied as predicted by RAT. In the synthetic *Planck* data the polarisation angles were again uniform, similar to the real G035.39-00.33 observation. The simulated POL-2 polarisation fractions were too low compared to the *Planck* values outside the filament. The discrepancy could be corrected by using a factor of 2 larger grains in the alignment calculations (Fig. 20). The observed high sub-millimetre opacity indicates some grain growth, which, however, is unlikely to be as large as a factor of 2. In reality, the effects of grain growth are more complex because also the grain shapes are probably affected.

In the more empirical modelling we simply assumed that grain alignment is lost above a certain volume density. The observed ratio of polarisation fractions was recovered when the threshold was $n(\mathrm{H_2}) \sim 10^4\,\mathrm{cm^{-3}}$. This would thus be consistent with no polarised intensity being emitted from the densest filament. The differences between the large-scale and the small-scale field morphologies would thus only probe the envelopes of the filament and the cores embedded within the filament (Appendix D).

6.2.3. Uncertainties of polarisation simulations

There are several caveats concerning the polarisation simulations and the comparison with the *Planck* and POL-2 observations.

In the modelling, the filtering of the POL-2 data was described using a simple high-pass filter. Figure 19 showed that the difference between filtering scales $\theta = 100''$ and $\theta = 200''$ was not significant. This is understandable because any high-pass filtering with a scale larger than the filament width will effectively remove all information of the uniform large-scale field. However, the actual filtering in POL-2 data reduction is not necessarily this simple. One needs simulations with the actual POL-2 reduction pipeline, to estimate the general effect of the filtering and to check for potential differences in the way the different Stokes vector components get processed.

The minimum size of the aligned grains and thus the polarisation reduction associated with RAT was calculated for the original grain size distributions of Compiègne et al. (2011) while the sub-millimetre emissivity was subsequently altered (see Sect. 3.3). A subsequent factor of 2 increase of the grain sizes had no effect on the simulated *Planck* values but increased the POL-2 polarisation fraction by ~30%. The total uncertainty related to the grain properties could be higher. The results depend not only on the grain size distribution but also on other poorly known factors that are related to the grain composition, grain shapes, and optical properties. Rather than an indication of specific dust opacities or grain sizes, the model comparison in Fig. 21 should only be taken as an indication of some of the uncertainties that affect the modelling of polarised dust emission.

Our models did not consider the effect of internal heating sources. While young stellar objects (YSOs) increase the radiation flux in their environment, this does not necessarily lead to significant enhancement of the observed polarisation. The angular momentum caused by the radiation reaches its maximum when radiation direction is aligned with the magnetic field (Hoang & Lazarian 2009). If the grain's angular momentum J is aligned with the magnetic field, only the RAT component projected onto the magnetic field direction is able to spin up the grain, leading to Eq. (38) of Hoang & Lazarian (2014): $J_{\mathrm{max}}^{\mathrm{RAT}}(\psi) = J_{\mathrm{max}}^{\mathrm{RAT}}(\psi = 0)\cos\psi$. If the aligning radiation is directed towards the observer, the angular momentum reaches its maximum when also the magnetic field is parallel to the observer's LOS. This leads to strong depolarisation, thanks to the $\cos^2\gamma$ term. On the other hand, for $\cos^2\gamma = 1$, $\cos\psi = 0$ and hence collisions are able to disrupt the grain alignment. Since RATs are effective mostly at UV and optical wavelengths, deeply embedded and already reddened YSOs may have an effect only in their immediate surroundings, which may correspond to a small part of the total dust along the LOS. Combined with the large beams of the sub-millimetre telescopes, the contribution of YSOs on the polarisation of distant clouds may thus remain negligible.

The comparison of the simulated *Planck* and POL-2 observations assumed that *Planck* is able to give an upper limit for the intrinsic polarisation. If the magnetic field had a strong random component, the p_{P} values observed with the large *Planck* beam would however underestimate this maximum polarisation fraction. Conversely, if line tangling were confined to the filament, a possibility also not probed by our models, this would lead to lower p in POL-2 observations. However, the RAT simulations appear to leave little room for additional geometrical depolarisation within the filament.

For the most part, our simulations assumed that the LOS magnetic field component is constant and similar both at large scales and within the filament. The ratio of the *Planck* and POL-2 values $p_{\mathrm{P}}/p_{\mathrm{S}}$ would be lower if the LOS field component was systematically larger outside the filament. For example, the large-scale field could be at 45° angles relative to the LOS while a toroidal field in the filament would make the field more perpendicular to the LOS towards the filament centre. Because the polarised intensity is proportional to $\cos^2\gamma$, the effect on the $p_{\mathrm{P}}/p_{\mathrm{S}}$ ratio would be a factor of 2. The effect would be quite significant and, if it were true, would even more strongly point to a complete loss of grain alignment inside the filament. Of course, the opposite situation where the field outside the filament is more closely aligned with the POS is in principle also possible.

The dust temperatures obtained from RT calculations contain some Monte Carlo noise but, once the temperature field is fixed, the I, Q, and U maps are mutually consistent to a very high accuracy. The simulated p values do not therefore suffer from noise bias but there are other uncertainties that are related to the underlying RT model. The intensity and the spectrum of the radiation field at the boundaries of the model volume affect especially the RAT calculations. Different assumptions of the dust sub-millimetre opacity were already seen to lead to models with different column densities and, consequently, different internal radiation fields. In Fig. 21, compared to the RT model with $\tau(250\ \mu\mathrm{m})/\tau(\mathrm{J}) = 1.6 \times 10^{-3}$, the assumption of $\tau(250\ \mu\mathrm{m})/\tau(\mathrm{J}) = 1.0 \times 10^{-3}$ lead to a 30% higher ratio of the *Planck* and POL-2 polarisation fractions. The continuum observations also do not give strong constraints on the volume densities. If we assumed the cloud to be more extended in the LOS direction, this would decrease the volume density and increase the short-wavelength radiation inside the cloud. Both factors would enhance grain alignment (see Eq. (14)). An inhomogeneous cloud structure would increase the penetration of the

external radiation but this would be partly compensated by the larger volume densities.

The best way to combat many of the listed uncertainties would be to study large samples of sources and use statistical arguments regarding the field orientation and the cloud shapes.

6.3. Field geometry vs. grain alignment

Planck studies have concluded that at large scales the relation between polarisation fraction p and column density N can be explained by the structure of the magnetic field without variations in the grain alignment. Planck Collaboration Int. XX (2015) found that the $p(N)$ relation was fairly well reproduced by MHD simulations with constant grain alignment but their observations only probed column densities up to $N(H_2) = 5 \times 10^{21}$ cm^{-2}. They refrained from drawing any conclusions for high column densities $N(H_2) > 10^{22}$ cm^{-2} for which also their MHD runs were not well suited. Soler et al. (2016) similarly concluded that at $N(H_2) < 5 \times 10^{21}$ cm^{-2} the polarisation angle dispersion and its relation to the polarisation fraction were mainly produced by fluctuations in the magnetic field structure.

Planck Collaboration XII (2018) examined in more detail the relationships between p, N, and S. The uniformity of the product $p \times S$ was noted as evidence that the drop in $p(N)$ is caused by the field structure rather than a loss of grain alignment. At a resolution of 40′, the $p(N)$ relation of Gould Belt clouds was followed up to $N(H_2) = 5 \times 10^{21}$ cm^{-2}. The probed linear scales were thus ∼1.6 pc for nearby clouds and ∼5 pc for Orion. The column densities are low because of the spatial resolution, which means that even towards the densest structures the polarised signal may be strongly affected by extended emission (usually with a higher polarisation fraction). However, with data at 10′ resolution, Fig. 21 in Planck Collaboration XII (2018) traces the product $p \times S$ up to $N(H_2) = 10^{23}$ cm^{-2}. The reduction of the grain alignment efficiency was estimated to be less than 25% between the diffuse ISM and the highest column densities. However, even at the highest column densities, the data do not exclusively probe the emission from regions of high volume density. Some drop in $p \times S$ was observed beyond $N(H_2) \sim 3 \times 10^{22}$ cm^{-2}. This was not very significant but, in principle, could hint at effects of reduced grain alignment being visible even in *Planck* data. Alternatively, this could be related to a qualitative change in the field morphology at scales dominated by the gravity.

These results are not directly comparable to our POL-2 study of the massive filament G035.39-00.33. Even with the higher angular resolution of POL-2 (0.56 pc for the 40″ angular resolution and the 2.9 Kpc distance), the filament is not fully resolved. However, the observed column densities, $N(H_2) > 10^{22}$ cm^{-2}, and especially the volume densities, are much higher than what is reached with *Planck*. Planck Collaboration Int. XX (2015) concluded that large column densities can be associated with low polarisation fraction especially because of the accumulation of many LOS structures. Our POL-2 observations target a single object that dominates the LOS column density. All extended emission also is already filtered out from the POL-2 data. For G035.39-00.33, the difference to the *Planck* data of the same region is particularly striking because of the low Galactic latitude (see Fig. 1).

Planck studies concluded was that their observations are *consistent* with constant grain alignment. Similarly, based on the POL-2 data and radiative transfer simulations, we can conclude that the observed $p(N)$ drop *can* be explained by the RAT mechanism alone, which even tends to overestimate the drop in p. The two conclusions are not necessarily contradictory. First, they apply to different parts of the ISM, POL-2 probing a source of much higher volume density. Second, the magnetic field geometry remains a significant source of uncertainty in our modelling and we cannot put a strict upper limit on its effects. For a single source, almost any $p(N)$ relation can be explained with a suitably crafted field geometry (small-scale structure or changes in the orientation relative to the LOS), without a need for variations in the grain alignment efficiency.

Another point of comparison is provided by the recent NIR polarimetry of the starless core FeSt 1-457 presented by Kandori et al. (2018). They did not observe any (significant) drop in the polarisation efficiency up to column densities of $A_V \sim 20$ mag. This is qualitatively in contradiction with the RAT predictions, although the authors noted that grain growth could provide at least a partial explanation. Furthermore, based on the extinction data discussed in Sect. 2.4, the extinction in the G035.39-00.33 field reaches significantly higher values. These are some $A_V \sim 50$ mag in both the northern and the southern clump, when measured at a resolution of 15″. Indeed, the comparison of a set of NIR and sub-millimetre polarisation observations lead Jones et al. (2015) to conclude that grain alignment is lost around $A_V \sim 20$ mag.

It is clear that even if grain alignment is partially lost, also the magnetic field orientation is never uniform and thus has some effect on the polarisation observations. To determine the relative importance of the two factors, we need more comparisons of high-resolution observations and simulations.

7. Conclusions

We have used *Planck*, *Herschel*, and SCUBA-2/POL-2 data to investigate dust emission and sub-millimetre polarisation in the G035.39-00.33 field. Our main conclusions are the following:

The ∼6 pc long main filament of the G035.39-00.33 field is characterised by dust colour temperatures $T \sim 12$–14 K and a column density in excess of $N(H_2) = 2 \times 10^{22}$ cm^{-2}.

The average sub-millimetre to NIR dust opacity ratio of the filament is $\tau(250\,\mu m)/\tau(J) = (2.55 \pm 0.03) \times 10^{-3}$. This is more than four times higher than in diffuse clouds and slightly higher than for previous samples of PGCC clumps of lower column density.

The average dust opacity spectral index of the filament is $\beta \sim 1.9$. This is similar to the values that previous studies have found for larger samples of PGCC clumps.

At large scales, *Planck* data show a relatively uniform magnetic field orientation but a polarisation fraction of only $p \sim 2\%$. The values of the polarisation angle dispersion function are on average $S(\delta \sim 2.5') \sim 9°$ and only slightly lower at the location of the G035.39-00.33 filament. The $S(p)$ relation was examined at resolutions between $FWHM = 5'$ and $FWHM = 15'$ and was found to be between the Planck Collaboration Int. XIX (2015) results (obtained at much larger scales) and a lower $S = 0.1/p$ relation.

POL-2 data reveal a very low polarisation fraction of $p \sim 1\%$ for the densest filament. The negative correlation between the polarisation fraction and column density is significant at $N(H_2) > 2 \times 10^{22}$ cm^{-2}.

Observations are consistent with models with an almost complete loss of grain alignment at densities above $n(H_2) \sim 10^4$ cm^{-3}. RAT calculations overestimate the decrease of polarised intensity, although this can be corrected by assuming a strong increase in grain sizes (a factor of 2). The modelling

is affected by large uncertainties in the grain properties, the magnetic field geometry (including the small-scale structure and the average LOS field component), and the underlying physical cloud model. Therefore, the relative importance of grain alignment and field geometry for the $p(N)$ relation remains open. High-resolution polarisation observations of a statistically significant sample of filaments, clumps, and cores are needed.

Acknowledgements. The *James Clerk Maxwell* Telescope is operated by the East Asian Observatory on behalf of The National Astronomical Observatory of Japan, Academia Sinica Institute of Astronomy and Astrophysics, the Korea Astronomy and Space Science Institute, the National Astronomical Observatories of China and the Chinese Academy of Sciences (Grant No. XDB09000000), with additional funding support from the Science and Technology Facilities Council of the United Kingdom and participating universities in the United Kingdom and Canada. Additional funds for the construction of SCUBA-2 were provided by the Canada Foundation for Innovation. The JCMT data were obtained under the programmes M16AL003 and M17BP050. *Planck* (http://www.esa.int/Planck) is a project of the European Space Agency – ESA – with instruments provided by two scientific consortia funded by ESA member states (in particular the lead countries: France and Italy) with contributions from NASA (USA), and telescope reflectors provided in a collaboration between ESA and a scientific consortium led and funded by Denmark. *Herschel* is an ESA space observatory with science instruments provided by European-led Principal Investigator consortia and with important participation from NASA. This research made use of Montage, funded by the National Aeronautics and Space Administration's Earth Science Technology Office, Computational Technologies Project, under Cooperative Agreement No. NCC5-626 between NASA and the California Institute of Technology. The code is maintained by the NASA/IPAC Infrared Science Archive. This research used the facilities of the Canadian Astronomy Data Centre operated by the National Research Council of Canada with the support of the Canadian Space Agency. We thank J. Kainulainen for providing the NIR/MIR extinction map used in the paper. M.J. and V.-M.P. acknowledge the support of the Academy of Finland Grant No. 285769. T.L. is supported by KASI fellowship and EACOA fellowship. V.-M.P. acknowledges the financial support from the European Research Council, Advanced Grant No. 320773 entitled Scattering and Absorption of Electromagnetic Waves in Particulate Media (SAEMPL). L.B. acknowledges support by CONICYT project Basal AFB-170002. W.K. was supported by Basic Science Research Program through the National Research Foundation of Korea (NRF-2016R1C1B2013642). C.W.L. was supported by Basic Science Research Program through the National Research Foundation of Korea (NRF) funded by the Ministry of Education, Science and Technology (NRF-2016R1A2B4012593). J.M. acknowledges the support of ERC-2015-STG No. 679852 RADFEEDBACK. The french co-authors thank the support from the Programme National Physique et Chimie du Milieu Interstellaire (PCMI) of CNRS/INSU with INC/INP co-funded by CEA and CNES.

References

Alina, D., Ristorcelli, I., Montier, L., et al. 2018, ArXiv e-prints [arXiv:1712.09325]
Alves, F. O., Franco, G. A. P., & Girart, J. M. 2008, A&A, 486, L13
Alves, F. O., Frau, P., Girart, J. M., et al. 2014, A&A, 569, L1
Alves, F. O., Frau, P., Girart, J. M., et al. 2015, A&A, 574, C4
Anathpindika, S., Burkert, A., & Kuiper, R. 2018, MNRAS, 474, 1277
André, P., Men'shchikov, A., Bontemps, S., et al. 2010, A&A, 518, L102
André, P., Di Francesco, J., Ward-Thompson, D., et al. 2014, Protostars and Planets VI, 27
Arzoumanian, D., André, P., Didelon, P., et al. 2011, A&A, 529, L6
Ballesteros-Paredes, J., Hartmann, L., & Vázquez-Semadeni, E. 1999, ApJ, 527, 285
Bally, J., Langer, W. D., Stark, A. A., & Wilson, R. W. 1987, ApJ, 312, L45
Beckwith, S. V. W., Sargent, A. I., Chini, R. S., & Guesten, R. 1990, AJ, 99, 924
Bernard, J.-P., Paradis, D., Marshall, D. J., et al. 2010, A&A, 518, L88
Bohlin, R. C., Savage, B. D., & Drake, J. F. 1978, ApJ, 224, 132
Bracco, A., Palmeirim, P., André, P., et al. 2017, A&A, 604, A52
Butler, M. J., & Tan, J. C. 2012a, ApJ, 754, 5
Butler, M. J., & Tan, J. C. 2012b, ApJ, 754, 5
Cardelli, J. A., Clayton, G. C., & Mathis, J. S. 1989, ApJ, 345, 245
Chen, C.-Y., King, P. K., & Li, Z.-Y. 2016a, ApJ, 829, 84
Chen, M. C.-Y., Di Francesco, J., Johnstone, D., et al. 2016b, ApJ, 826, 95
Compiègne, M., Verstraete, L., Jones, A., et al. 2011, A&A, 525, A103
Cox, N. L. J., Arzoumanian, D., André, P., et al. 2016, A&A, 590, A110
del Burgo, C., & Laureijs, R. J. 2005, MNRAS, 360, 901
Dempsey, J. T., Friberg, P., Jenness, T., et al. 2013, MNRAS, 430, 2534
Drabek, E., Hatchell, J., Friberg, P., et al. 2012, MNRAS, 426, 23
Egan, M. P., Shipman, R. F., Price, S. D., et al. 1998, ApJ, 494, L199
Elmegreen, D. M., & Elmegreen, B. G. 1979, AJ, 84, 615
Federrath, C., Roman-Duval, J., Klessen, R. S., Schmidt, W., & Mac Low M.-M. 2010, A&A, 512, A81
Fernández-López, M., Arce, H. G., Looney, L., et al. 2014, ApJ, 790, L19
Fissel, L. M., Ade, P. A. R., Angilé, F. E., et al. 2016, ApJ, 824, 134
Gerakines, P. A., Whittet, D. C. B., & Lazarian, A. 1995, ApJ, 455, L171
Goodman, A. A., Bastien, P., Menard, F., & Myers, P. C. 1990, ApJ, 359, 363
Goodman, A. A., Jones, T. J., Lada, E. A., & Myers, P. C. 1995, ApJ, 448, 748
Goodman, A. A., Alves, J., Beaumont, C. N., et al. 2014, ApJ, 797, 53
Gordon, K. D., Baes, M., Bianchi, S., et al. 2017, A&A, 603, A114
Griffin, M. J., North, C. E., Schulz, B., et al. 2013, MNRAS, 434, 992
Hacar, A., Tafalla, M., Kauffmann, J., & Kovács, A. 2013, A&A, 554, A55
Hacar, A., Tafalla, M., Forbrich, J., et al. 2018, A&A, 610, A77
Hennebelle, P., Banerjee, R., Vázquez-Semadeni, E., Klessen, R. S., & Audit, E. 2008, A&A, 486, L43
Hennemann, M., Motte, F., Schneider, N., et al. 2012, A&A, 543, L3
Henshaw, J. D., Jiménez-Serra, I., Longmore, S. N., et al. 2017, MNRAS, 464, L31
Heyer, M. H., Vrba, F. J., Snell, R. L., et al. 1987, ApJ, 321, 855
Heyer, M., Goldsmith, P. F., Yıldız, U. A., et al. 2016, MNRAS, 461, 3918
Hill, T., Motte, F., Didelon, P., et al. 2011, A&A, 533, A94
Hoang, T., & Lazarian, A. 2009, ApJ, 697, 1316
Hoang, T., & Lazarian, A. 2014, MNRAS, 438, 680
Holland, W. S., Bintley, D., Chapin, E. L., et al. 2013, MNRAS, 430, 2513
Hoq, S., Clemens, D. P., Guzmán, A. E., & Cashman, L. R. 2017, ApJ, 836, 199
Jones, T. J., Klebe, D., & Dickey, J. M. 1992, ApJ, 389, 602
Jones, T. J., Bagley, M., Krejny, M., Andersson, B.-G., & Bastien, P. 2015, AJ, 149, 31
Juvela, M. 2018, A&A, submitted
Juvela, M., & Ysard, N. 2012a, A&A, 541, A33
Juvela, M., & Ysard, N. 2012b, A&A, 539, A71
Juvela, M., Ristorcelli, I., Pagani, L., et al. 2012, A&A, 541, A12
Juvela, M., Malinen, J., & Lunttila, T. 2013a, A&A, 553, A113
Juvela, M., Montillaud, J., Ysard, N., & Lunttila, T. 2013b, A&A, 556, A63
Juvela, M., Demyk, K., Doi, Y., et al. 2015a, A&A, 584, A94
Juvela, M., Ristorcelli, I., Marshall, D. J., et al. 2015b, A&A, 584, A93
Juvela, M., He, J., Pattle, K., et al. 2018, A&A, 612, A71
Kainulainen, J., & Tan, J. C. 2013, A&A, 549, A53
Kainulainen, J., Alves, J., Beuther, H., Henning, T., & Schuller, F. 2011, A&A, 536, A48
Kandori, R., Tamura, M., Nagata, T., et al. 2018, ApJ, 857, 100
Klassen, M., Pudritz, R. E., & Kirk, H. 2017, MNRAS, 465, 2254
Koch, P. M., Tang, Y.-W., Ho, P. T. P., et al. 2014, ApJ, 797, 99
Kramer, C., Richer, J., Mookerjea, B., Alves, J., & Lada, C. 2003, A&A, 399, 1073
Kwon, J., Doi, Y., Tamura, M., et al. 2018, ApJ, 859, 4
Lawrence, A., Warren, S. J., Almaini, O., et al. 2007, MNRAS, 379, 1599
Lazarian, A., & Hoang, T. 2007, MNRAS, 378, 910
Lazarian, A., Goodman, A. A., & Myers, P. C. 1997, ApJ, 490, 273
Lehtinen, K., Russeil, D., Juvela, M., Mattila, K., & Lemke, D. 2004, A&A, 423, 975
Li, J. I., Liu, H. B., Hasegawa, Y., & Hirano, N. 2017, ApJ, 840, 72
Li, P. S., Klein, R. I., & McKee, C. F. 2018, MNRAS, 473, 4220
Liu, T., Kim, K.-T., Juvela, M., et al. 2018a, ApJS, 234, 28
Liu, T., Li, P. S., Juvela, M., et al. 2018b, ApJ, 859, 151
Lombardi, M., & Alves, J. 2001, A&A, 377, 1023
Mairs, S., Johnstone, D., Kirk, H., et al. 2015, MNRAS, 454, 2557
Mairs, S., Johnstone, D., Kirk, H., et al. 2016, MNRAS, 461, 4022
Malinen, J., Juvela, M., Collins, D. C., Lunttila, T., & Padoan, P. 2011, A&A, 530, A101
Malinen, J., Montier, L., Montillaud, J., et al. 2016, MNRAS, 460, 1934
Martin, P. G., Roy, A., Bontemps, S., et al. 2012, ApJ, 751, 28
Mathis, J. S., Mezger, P. G., & Panagia, N. 1983, A&A, 128, 212
Matthews, T. G., Ade, P. A. R., Angilé, F. E., et al. 2014, ApJ, 784, 116
Men'shchikov, A. 2016, A&A, 593, A71
Men'shchikov, A., André, P., Didelon, P., et al. 2010, A&A, 518, L103
Miettinen, O. 2018, A&A, 609, A123
Montier, L., Plaszczynski, S., Levrier, F., et al. 2015a, A&A, 574, A135
Montier, L., Plaszczynski, S., Levrier, F., et al. 2015b, A&A, 574, A136
Moore, T. J. T., Plume, R., Thompson, M. A., et al. 2015, MNRAS, 453, 4264
Motte, F., Zavagno, A., Bontemps, S., et al. 2010, A&A, 518, L77
Neha, S., Maheswar, G., Soam, A., & Lee, C. W. 2018, MNRAS, 476, 4442
Nguyen Luong, Q., Motte, F., Hennemann, M., et al. 2011, A&A, 535, A76

Padoan, P., Juvela, M., Goodman, A. A., & Nordlund, Å. 2001, ApJ, 553, 227
Pagani, L., Lefèvre, C., Juvela, M., Pelkonen, V.-M., & Schuller, F. 2015, A&A, 574, L5
Palmeirim, P., André, P., Kirk, J., et al. 2013, A&A, 550, A38
Pattle, K., Ward-Thompson, D., Kirk, J. M., et al. 2015, MNRAS, 450, 1094
Pattle, K., Ward-Thompson, D., Berry, D., et al. 2017, ApJ, 846, 122
Pelkonen, V.-M., Juvela, M., & Padoan, P. 2009, A&A, 502, 833
Pereyra, A., & Magalhães, A. M. 2004, ApJ, 603, 584
Planck Collaboration XI. 2014, A&A, 571, A11
Planck Collaboration I. 2016, A&A, 594, A1
Planck Collaboration XXVIII. 2016, A&A, 594, A28
Planck Collaboration XII. 2018, A&A submitted [arXiv:1807.06212]
Planck Collaboration Int. XIV. 2014, A&A, 564, A45
Planck Collaboration Int. XVII. 2014, A&A, 566, A55
Planck Collaboration Int. XIX. 2015, A&A, 576, A104
Planck Collaboration Int. XX. 2015, A&A, 576, A105
Planck Collaboration Int. XXIX. 2016, A&A, 586, A132
Planck Collaboration Int. XXXII.. 2016, A&A, 586, A135
Planck Collaboration Int. XXXIII. 2016, A&A, 586, A136
Planck Collaboration Int. XXXV. 2016, A&A, 586, A138
Plaszczynski, S., Montier, L., Levrier, F., & Tristram, M. 2014, MNRAS, 439, 4048
Poglitsch, A., Waelkens, C., Geis, N., et al. 2010, A&A, 518, L2
Ridderstad, M., & Juvela, M. 2010, A&A, 520, A18
Rivera-Ingraham, A., Ristorcelli, I., Juvela, M., et al. 2016, A&A, 591, A90
Roy, A., Martin, P. G., Polychroni, D., et al. 2013, ApJ, 763, 55
Santos, F. P., Busquet, G., Franco, G. A. P., Girart, J. M., & Zhang, Q. 2016, ApJ, 832, 186
Schneider, N., Csengeri, T., Hennemann, M., et al. 2012, A&A, 540, L11
Shetty, R., Kauffmann, J., Schnee, S., & Goodman, A. A. 2009a, ApJ, 696, 676
Shetty, R., Kauffmann, J., Schnee, S., Goodman, A. A., & Ercolano, B. 2009b, ApJ, 696, 2234
Simon, R., Rathborne, J. M., Shah, R. Y., Jackson, J. M., & Chambers, E. T. 2006, ApJ, 653, 1325
Soler, J. D., Hennebelle, P., Martin, P. G., et al. 2013, ApJ, 774, 128
Soler, J. D., Alves, F., Boulanger, F., et al. 2016, A&A, 596, A93
Stepnik, B., Abergel, A., Bernard, J., et al. 2003, A&A, 398, 551
Suutarinen, A., Haikala, L. K., Harju, J., et al. 2013, A&A, 555, A140
Svoboda, B. E., Shirley, Y. L., Battersby, C., et al. 2016, ApJ, 822, 59
Voshchinnikov, N. V., Das, H. K., Yakovlev, I. S., & Il'in, V. B. 2013, Astron. Lett., 39, 421
Vrba, F. J., Strom, S. E., & Strom, K. M. 1976, AJ, 81, 958
Wang, K., Testi, L., Ginsburg, A., et al. 2015, MNRAS, 450, 4043
Ward-Thompson, D., Kirk, J. M., Crutcher, R. M., et al. 2000, ApJ, 537, L135
Webb, K. A., Di Francesco, J., Sadavoy, S., et al. 2017, ApJ, 849, 13
Whittet, D. C. B., Gerakines, P. A., Hough, J. H., & Shenoy, S. S. 2001, ApJ, 547, 872
Wright, E. L., Eisenhardt, P. R. M., Mainzer, A. K., et al. 2010, AJ, 140, 1868
Wu, B., Tan, J. C., Christie, D., et al. 2017, ApJ, 841, 88
Ysard, N., Juvela, M., Demyk, K., et al. 2012, A&A, 542, A21
Ysard, N., Abergel, A., Ristorcelli, I., et al. 2013, A&A, 559, A133
Zhang, C.-P., Yuan, J.-H., Li, G.-X., Zhou, J.-J., & Wang, J.-J. 2017, A&A, 598, A76

Appendix A: Modified black-body fit to maps of different resolution

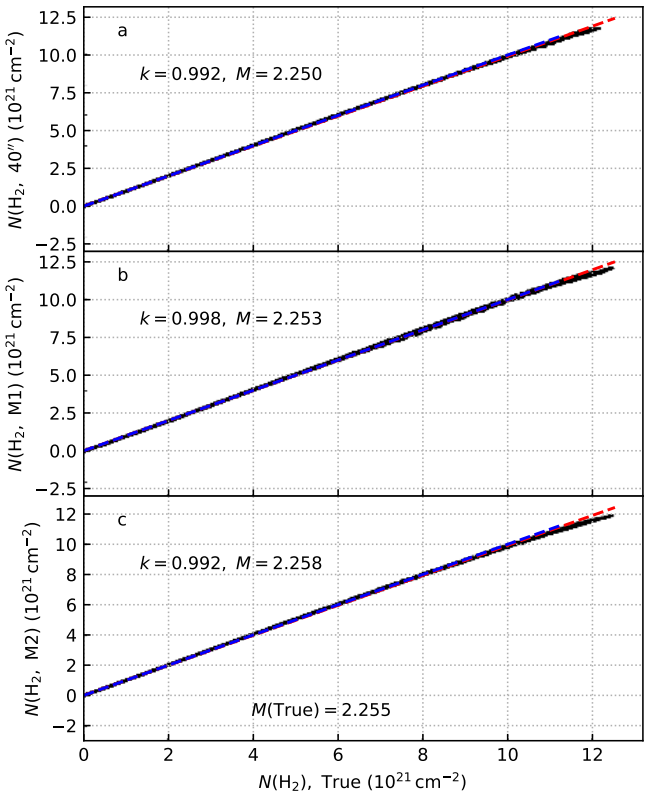

Fig. A.1. Correlations of column density estimates for the externally heated, lower column density model. The x-axis is the true column density of the model cloud at the resolution of 40″ (*panel a*) or 18″ (*panels b and c*). On the y-axes are the results from direct MBB fits at 40″ resolution (*panel a*) and from methods A and B at 18″ resolution (*panels b and c*, respectively). The dashed blue lines show the one-to-one relations and the dashed red lines the least squares fits. The slopes k of the least squares lines as well as the estimated cloud masses (in solar masses) are given in the panels. The true mass of the cloud is quoted in *panel c*.

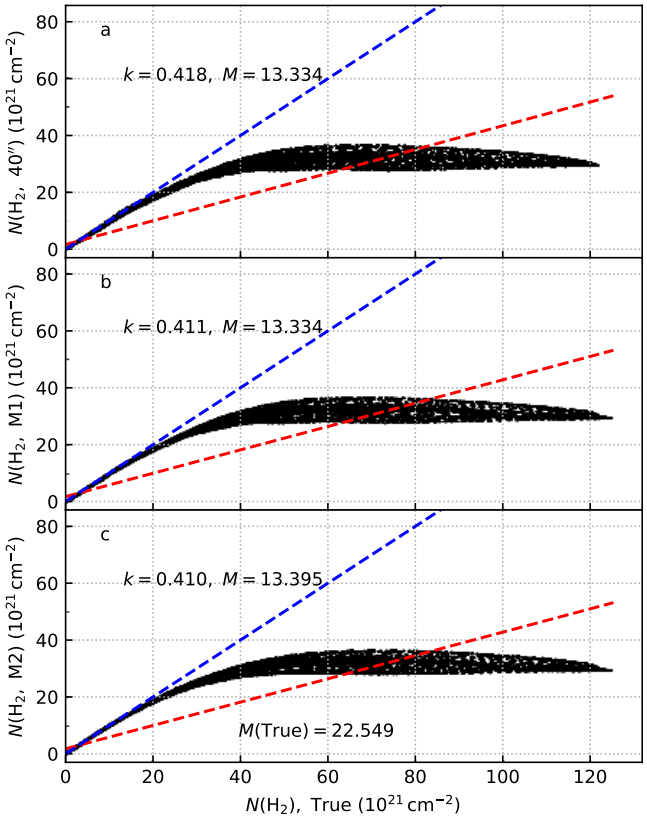

Fig. A.2. Same as Fig.A.1 but for the higher column density model.

Section 3.1 described how column density can be estimated using surface brightness maps that are first convolved down to a common resolution. The resolution can be increased in several ways. Palmeirim et al. (2013) employed different combinations of the observed bands. All bands were first used to derive a column density map N_0 at the lowest common resolution. The lowest resolution bands are then removed one by one and the remaining bands are used to calculate corrections for higher spatial frequencies. On each step a new map is obtained as

$$\hat{N}_i = \hat{N}_{i-1} + \mathrm{HPF}(N_i, FWHM_{i-1}), \quad \text{(A.1)}$$

where $\hat{N}_{i-1}$ is the previous estimate at the resolution $FWHM_{i-1}$. N_i is a resolution $FWHM_i$ map that is calculated using the maps that have a resolution better or equal to $FWHM_i$, all convolved to $FWHM_i$. HPF stands for high-pass filtering for the indicated beam size. In the following, we refer to this as method A.

In Sect. 4.1 we made high-resolution column density maps by constructing a model that consisted of high-resolution maps of temperature and surface brightness at a reference frequency. The model was optimised by comparing its predictions with the observed surface brightness maps, each at its original resolution. This procedure (in the following method B) is time-consuming because each optimisation step involves convolutions. The model parameters also are not independent between pixels and must be solved simultaneously. After optimisation, the model maps can be converted to a column density map. The nominal resolution could be even higher than in method A but regularisation may be needed to avoid oscillations that are typical for deconvolution. The pixel size of the model maps must be small compared to the resolution of the observations. In Sect. 4.1, the best resolution of observations was 18″, the model was defined 6″ pixels, and the final result was at a resolution of 20″. As regularisation, we compared the model surface brightness and temperature values X to the average of its immediate neighbours ($\hat{X}$) and added to the χ^2 values a penalty $\xi(X - \hat{X})/\hat{X})^2$ with a small weight factor ξ = 0.005. Without regularisation χ^2 values would be better but larger small-scale temperature fluctuations could lead to a higher average column density. This shows that analysis of surface brightness data is not unique. The assumption of a minimal amount of structure below the observed resolution is a special case that leads to the lowest column density values.

In method A, the highest spatial frequencies depend on the pair of surface brightness maps with the highest resolution. Because method B solves a global optimisation problem, the role of different bands in constraining structures at different scales could be different, also because shorter wavelengths are more sensitive to temperature variations (e.g. Shetty et al. 2009b; Malinen et al. 2011).

We tested the methods using surface brightness maps obtained from radiative transfer modelling. The density distributions of the model clouds followed a 3D Gaussian distribution to which we had added minor Gaussian fluctuations. The peak column densities were either $N(\mathrm{H_2}) = 1.3 \times 10^{22}$ cm^{-2} or a value 10 times higher. The models were heated by external radiation and,

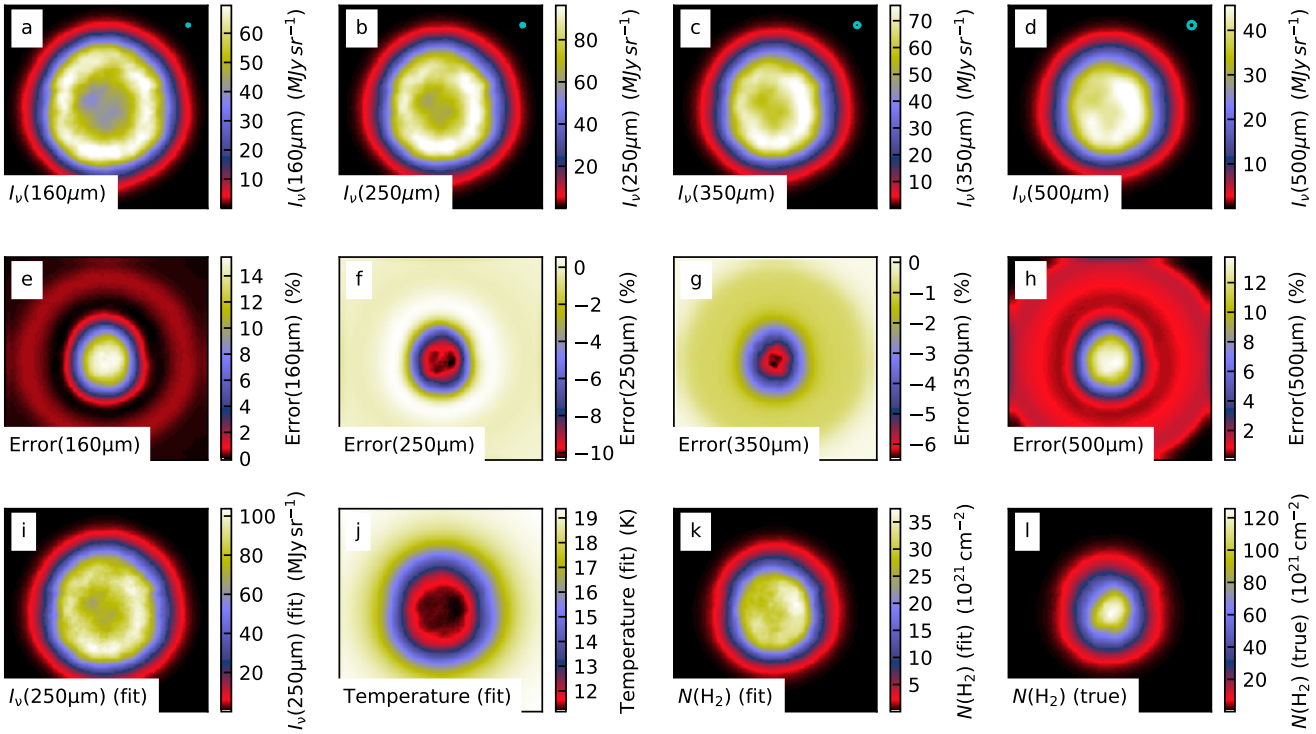

Fig. A.3. Fit of the simulated observations of the high-column-density model without observational noise. The first row shows the synthetic surface brightness maps with the beam size indicated in the upper right corner. The second row shows the relative fit residuals. *Panels i and j* show the fitted model parameters, the 250 μm surface brightness and the colour temperature. *Panels k and l* compare the final column density map at 10″ resolution to the true column density.

optionally, with a few internal black-body sources that raised the dust temperature locally to ~100 K. We used the (Mathis et al. 1983) model of the interstellar radiation field and the dust model of Compiègne et al. (2011). Radiative transfer computations were used to solve the 3D temperature distributions and to provide surface brightness maps at 160, 250, 350, and 500 μm. The 160 μm band was included to increase the sensitivity to temperature variations. We used the radiative transfer programme SOC (Juvela et al., in prep.; Gordon et al. 2017), describing the volume discretisation with hierarchical grids that were refined according to the volume density. The effective resolution was 1024^3 cells and the total number of cells some 54 millions. The synthetic observations and the subsequent analysis assume Gaussian beams that correspond to the resolutions of the *Herschel* 160–500 μm bands. We used observational uncertainties of 5% for the 160 μm band and 3.5% for the other bands. The column densities estimated with the methods A and B were compared to the true column densities of the model clouds. The analysis assumed a spectral index value of $\beta = 1.8$. The spectral index of the dust model is slightly different and, therefore, we apply to the calculated column densities a correction factor that in the case of an isothermal model results in estimates equal to the true column density.

Figure A.1 shows results for the lower column density model with only external illumination and without observational noise. The figure also includes column density estimates calculated from data convolved to 40″. One pixel of the radiative transfer model corresponded to 1″, which means that structures are well resolved. All estimates are in good agreement with the true column density values.

The situation is different for the high column density model (Fig. A.2). The column densities are severely underestimated

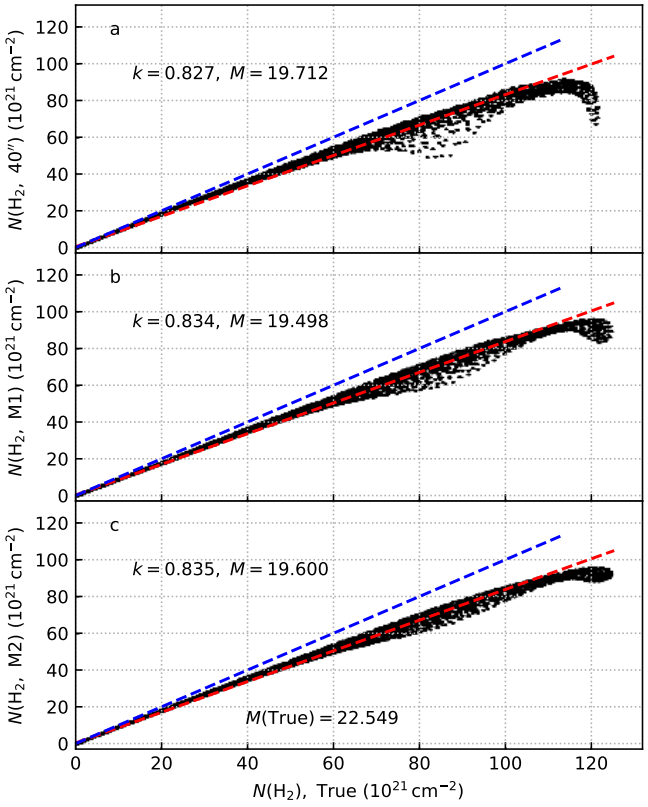

Fig. A.4. As Fig.A.2, but with added internal heating sources.

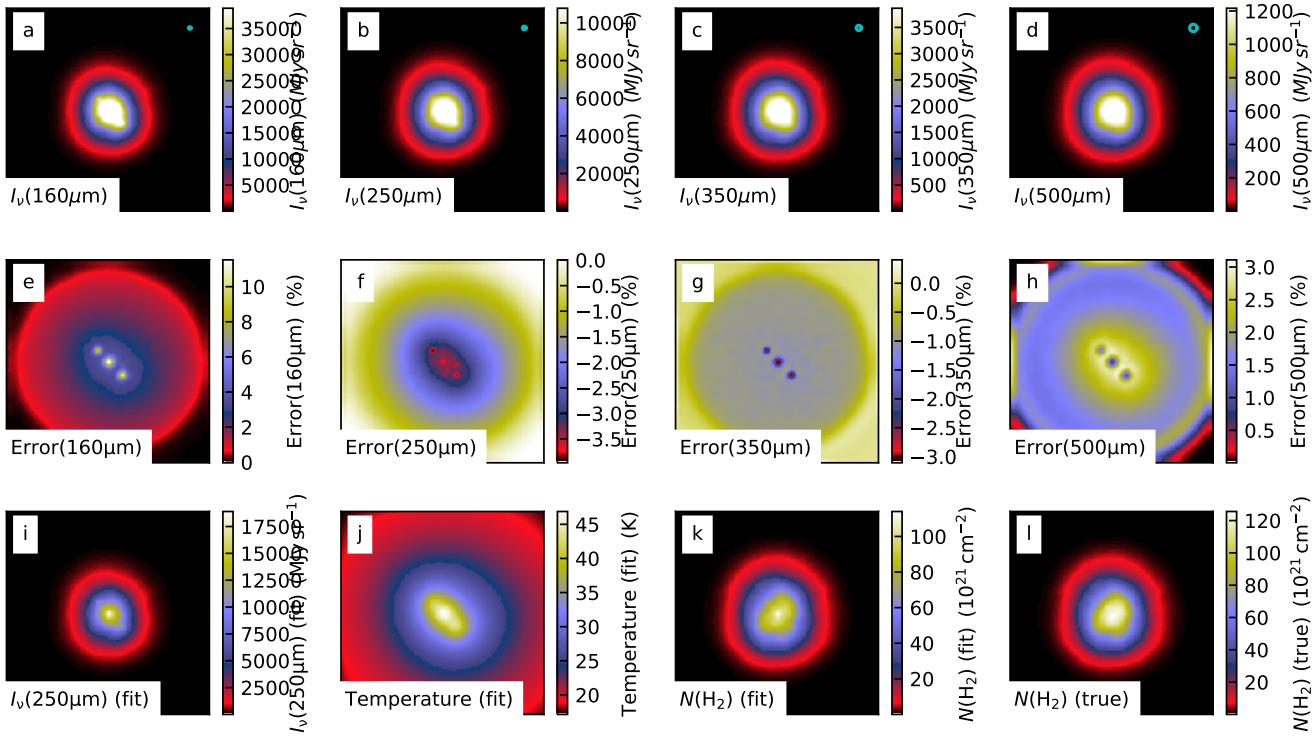

Fig. A.5. As Fig. A.3 but with added internal heating sources.

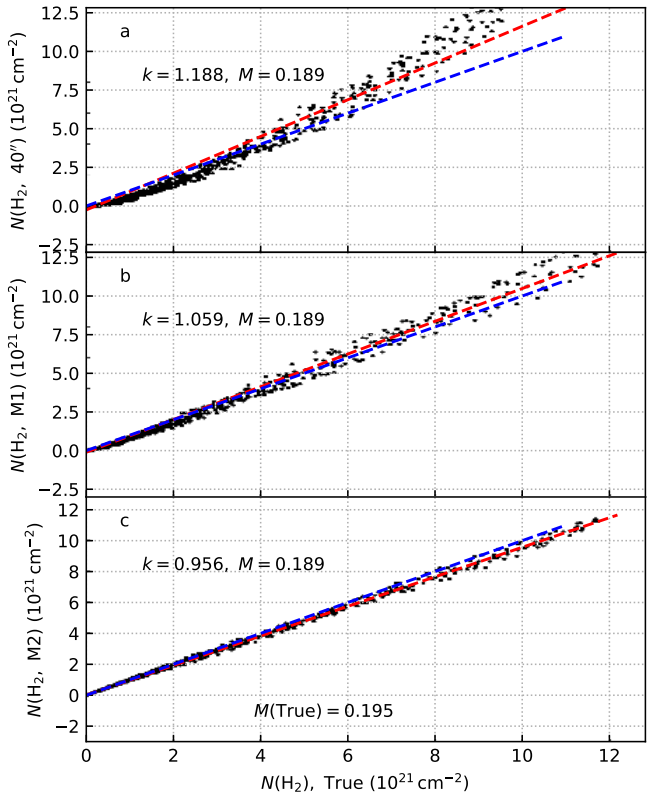

Fig. A.6. As Fig. A.1 but with a factor of 3 lower spatial resolution and with added observational noise. In each panel, the lower right corner shows the zoom-in to a column density range from 0 to 10^{21} cm^{-2}. The rms dispersion relative to the linear least squares fit is indicated in each panel.

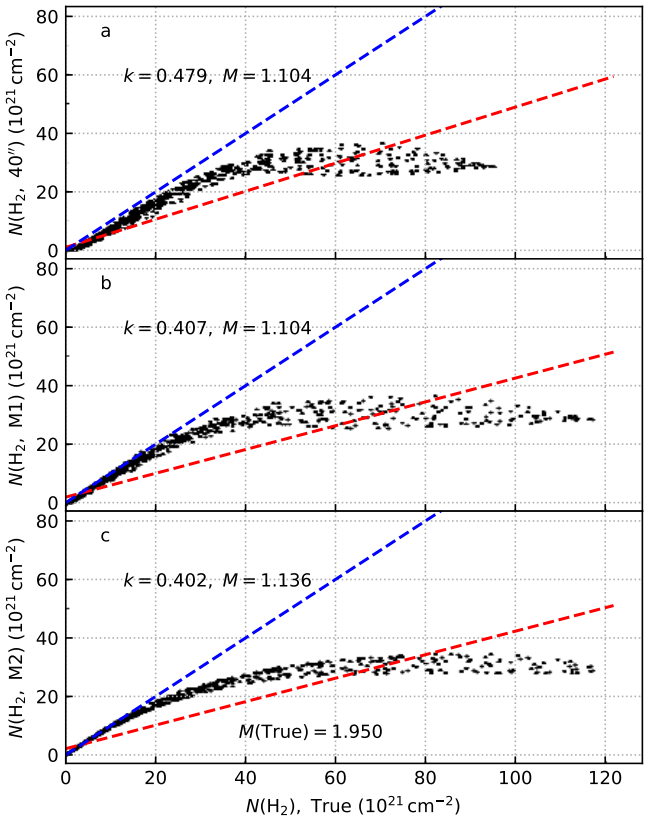

Fig. A.7. As Fig. A.6 but for the models with higher column density. Compared to Fig. A.4, the spatial resolution is lower by a factor of 3 and the data include added observational noise.

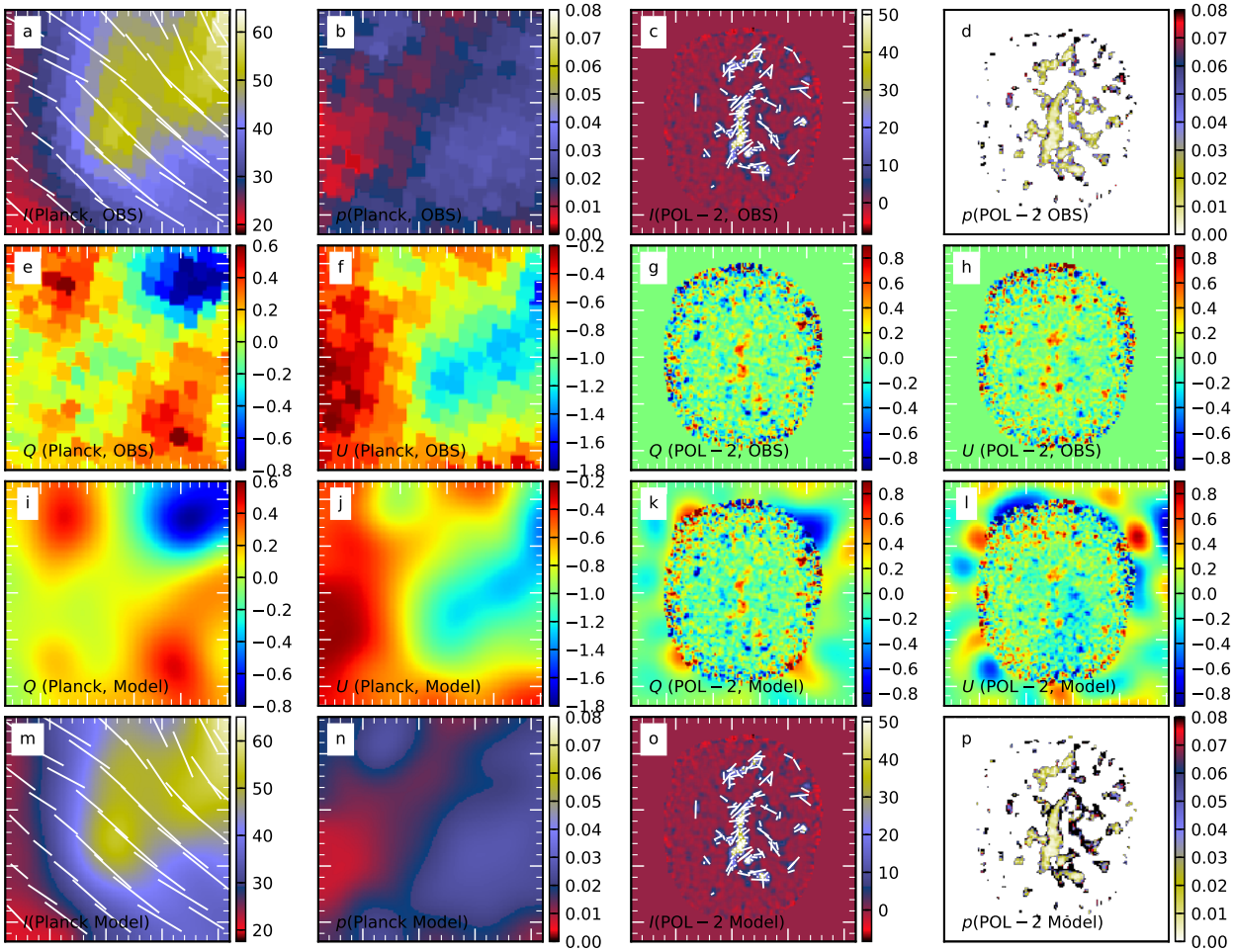

Fig. B.1. Results for the combined (I, Q, U) fir to *Planck* and POL-2 data. *Panels a–d* show the observed *Planck* and POL-2 surface brightness data and polarisation fraction maps. *Panels a and c*: the polarisation vectors based on observations. The second row shows the observed *Planck* and POL-2 maps of Q and U. The third and fourth rows show the (I, Q, U) maps of the fitted model. In *panels c and o* polarisation vectors are drawn only in regions with I (850 μm) > 5 mJy sr^{-1}.

above $N(\mathrm{H_2}) = 2 \times 10^{22}$ cm^{-2}. The estimates are actually decreasing towards the highest column densities and the maximum error is close a factor of 4. The methods A and B give practically identical results. Figure A.3 shows the method B fit in the form of maps. Because of LOS temperature variations, the observed spectrum is much wider than the best-fit MBB function, and the maximum residuals exceed 10% of the measured surface brightness.

Figures A.4 and A.5 show the results for the high-column-density model after the addition of internal sources. At the highest column densities method B now results in marginally higher column density estimates than method A. Although the presence of internal heating has significantly reduced the bias, both methods underestimate the true column density by up to 25%. The point sources are barely resolved. If the resolution of the observations is degraded by a factor of 3, the results of the methods A and B are identical.

We repeated the tests after adding to the synthetic observations Gaussian noise equal to the error estimates of the observations. Figures A.6 and A.7 show the results for lower resolution observations where the original model pixel corresponds to 0.3′. For the lower column density model the differences are not significant, although the scatter of the $N(\mathrm{H_2})$ estimates is marginally smaller for method B (Fig. A.6). The results at higher column densities (Fig. A.7) are qualitatively similar to those without noise (Fig. A.2). Method B again exhibits slightly smaller dispersion, especially at low column densities. This is due to the global nature of the solution with some additional effect from the regularisation. Apart from this, the results of the two methods are in practice identical.

Appendix B: Fit of the (*I*, *Q*, *U*) data of *Planck* and POL-2

Because of the *Planck* and JCMT POL-2 polarisation maps, we tested their consistency by making a model that consisted of (I, Q, U) maps. These model maps were optimised through comparison with the *Planck* and POL-2 observations, both at their original resolutions. In the case of POL-2, the filtering of low spatial frequencies was simulated by subtracting a map obtained by convolving the observations with a Gaussian beam with θ = 300″. In the main text, the filtering was assumed to be stronger with θ = 200″ and this would make it even easier to reconcile any differences between the instruments. The model (I, Q, U) maps had a pixel size of 10″. The model optimisation took into account the error estimates (see Sect. 2) and the degree to which the model was oversampled compared to the observations.

The results are shown in Fig. B.1. The obtained (I, Q, U) images fit well both the *Planck* and POL-2 data. In spite of the

uncertainties (for example, the true nature of POL-2 filtering), the exercise shows that there is no discrepancy between the data sets but also that the spatial filtering plays a major role in the magnetic field morphology seen in the POL-2 data.

Appendix C: Effect of noise on the relations between *p*, *N*, and *S*

Noise affects the estimated values of both polarisation angles and polarisation fraction (e.g. Montier et al. 2015a; Fissel et al. 2016). In the following, we use simulations to estimate the effect of noise on the observed relations between polarisation fraction, column density, and polarisation angle dispersion function. In the case of polarisation fraction, we always refer to $p_{\rm mas}$ estimates that are already corrected for bias, as described in Sect. 3.2. The correction is reliable at $p_{\rm mas}/\sigma_{p,{\rm mas}} > 2$ but values at lower S/N can be expected to be biased (Montier et al. 2015b). However, even biased data contain some information, which can be used when data are compared to simulated observations.

Figure 13 showed a negative correlation between the $p_{\rm mas}$ and S values estimated from *Planck* data. Such a trend could result from noise if that causes significant bias in the polarisation fraction estimates. For comparison with Fig. 13, we made a simulation using the average error estimates of the *Planck* data (including the covariances) but assuming constant values for both polarisation angles and polarisation fractions. The results are shown in Fig. C.1. At full *Planck* resolution, noise increases the typical S values that, nevertheless, are only a fraction of the values in Fig. 13. The polarisation fraction estimates show some dispersion but the values are unbiased. As a result, the $p_{\rm mas}(S)$ relation shows no significant correlations, unlike in the actual observations shown in Fig. 13c.

We examined the $p_{\rm mas}$ vs. N relation of POL-2 data as a function of the resolution. Lower resolution may increase geometrical depolarisation but, more importantly, increases the S/N and thus reduces the noise bias. In Fig. C.2, we plot $p_{\rm mas}$ as a function of column density at the resolutions of 20″, 40″, and 80″. Only data with $N({\rm H_2}) > 7.5 \times 10^{21}\,{\rm cm^{-2}}$ are used for linear fits. As the resolution is reduced, the slope decreases. Above $N({\rm H_2}) \sim 20 \times 10^{21}\,{\rm cm^{-2}}$ the polarisation fraction is nevertheless 1–2%, irrespective of the resolution.

For comparison with Fig. C.2, Fig. C.3 shows simulations of the $p_{\rm mas}$ vs. N relation in the presence of noise. The simulations assumed that the true polarisation fraction is constant 1.5% and the observed p depends on the column density only because of the noise bias. The observed intensity was assumed to be directly proportional to the column density. The S/N of the total intensity at $N({\rm H_2}) = 10^{22}\,{\rm cm^{-2}}$ is either 40 or 100. In the observations, the S/N is not constant for a given column density and the values at $N({\rm H_2}) = 10^{22}\,{\rm cm^{-2}}$ range from $S/N \sim 10$ to $S/N \sim 70$ with a mean value of ∼33. Thus, the $S/N = 100$ simulation could define a lower envelope for $p_{\rm mas}$, the observed values being higher because of the noise bias. Above $N({\rm H_2}) = 2 \times 10^{22}\,{\rm cm^{-2}}$, the average S/N is $S/N \sim 100$ or higher (see Fig. C.2).

In Fig. C.3, when the data are convolved to a lower resolution, the S/N increases and the $p_{\rm mas}$ values decrease. Eventually, the high-$N({\rm H_2})$ values become independent of the convolution while the polarisation fractions still decrease at lower $N({\rm H_2})$. At 40″ resolution, p values become reliable only at $N({\rm H_2}) > 10^{22}\,{\rm cm^{-2}}$, where the average S/N of observations is above 100 for the total intensity.

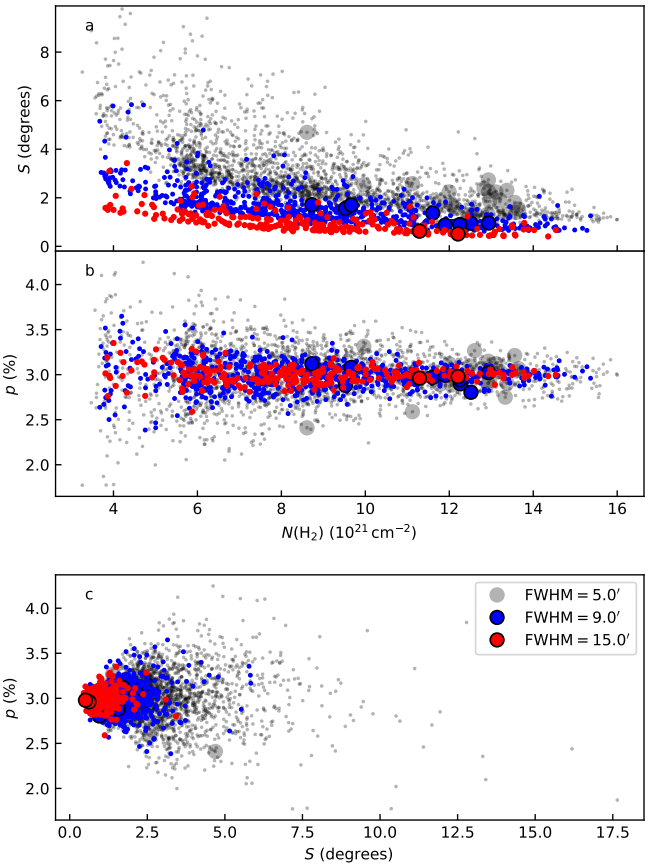

Fig. C.1. Polarisation angle dispersion function S and polarisation fraction $p_{\rm mas}$ based on simulated *Planck* data that assume a constant polarisation angle and a constant polarisation fraction of 3%. *Panels a and b* show these as a function of dust optical depth and *panel c* shows their mutual correlation. The colours correspond to the data resolution, as indicated in *panel c*. The points inside the area mapped with POL-2 are plotted with large symbols. The data are sampled at steps of *FWHM*/2 and S is calculated for lag δ = *FWHM*/2.

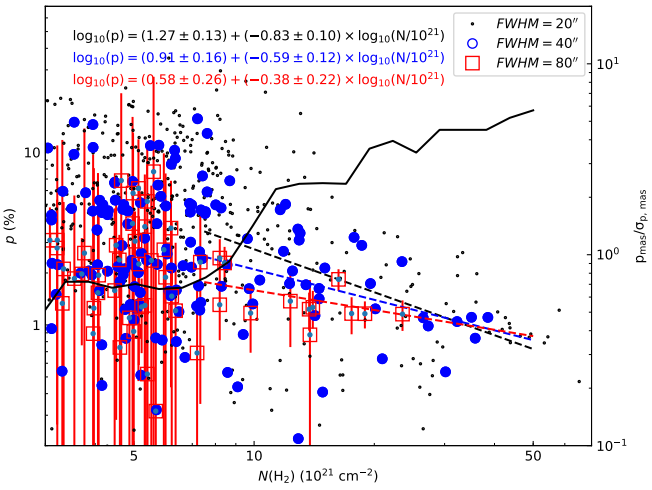

Fig. C.2. Polarisation fraction $p_{\rm mas}$ as a function of column density, based on POL-2 data at 20″, 40″, and 80″ resolution. The data are sampled at half-beam steps. The dashed lines correspond to least squares fits data $N({\rm H_2}) > 7.5 \times 10^{21}\,{\rm cm^{-2}}$. The error bars are shown only for the *FWHM* = 80″ data points. The solid black line and the right-hand y-axis show the median S/N for polarisation fraction, $p_{\rm mas}/\sigma_{p,{\rm mas}}$, at 40″ resolution.

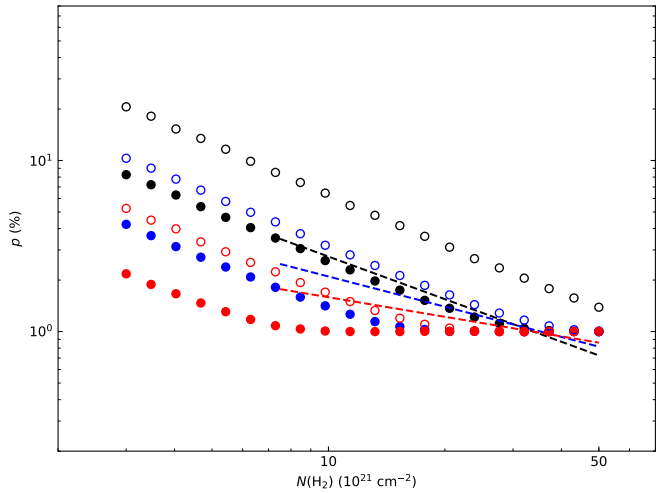

Fig. C.3. Simulations of the $p_{\rm mas}$ vs. N relations in POL-2 observations. The calculations assumed a regular field (no geometrical depolarisation), an intrinsic polarisation fraction of $p = 1\%$, and intensities proportional to the column density. The initial S/N of the total intensity at $N(H_2) = 10^{22}$ cm^{-2} at the full $FWHM = 15''$ resolution is either 40 (open circles) or 200 (solid circles). The black, blue, and red colours correspond to the convolution to a resolution of $20''$, $40''$, and $80''$, respectively. For comparison, the dashed lines show the least squares fits from Fig. C.2.

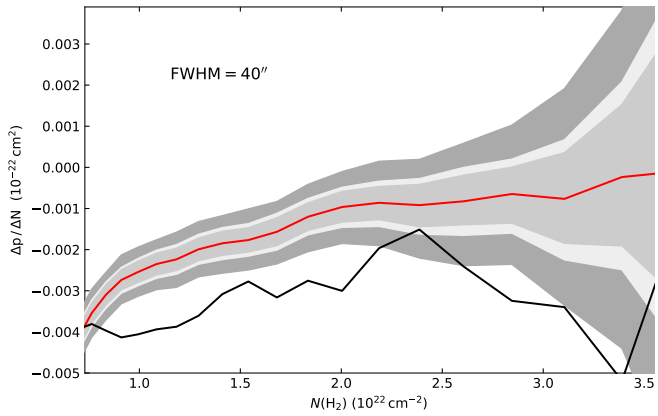

Fig. C.4. Simulation of $p_{\rm mas}$ vs. N relation for POL-2 data. The figure shows the slopes of the fitted least squares lines as a function of the column density threshold used to select data. The black line shows the fits to the original observations. The red curve shows the median slope for simulations that assume an intrinsically constant polarisation fraction of $p = 1.5\%$ and the shaded areas correspond to [1%, 99%], [10%, 90%], and [16%, 84%] confidence intervals.

In Fig. 14 we concluded that the anti-correlation would be true, based on the S/N of the selected data (Fig. 9) and the formal errors of the fitted least squares lines. We examined this more directly using the observed (I, Q, U) data and their error estimates. We rescaled (Q, U) so that they corresponded to a flat relation $p = 1.5\%$. We constructed synthetic data sets where noise was added according to the POL-2 error maps and the $p_{\rm mas}(N)$ relation was fitted with a weighted least squares line. The simulation was repeated 2000 times for a number of column density thresholds. Figure C.4 indicates that there is over 99% probability that the observed slope is steeper than what is expected based on the constant-p assumption. The slopes become uncertain for thresholds $N(H_2) > 3 \times 10^{22}$ cm^{-2}

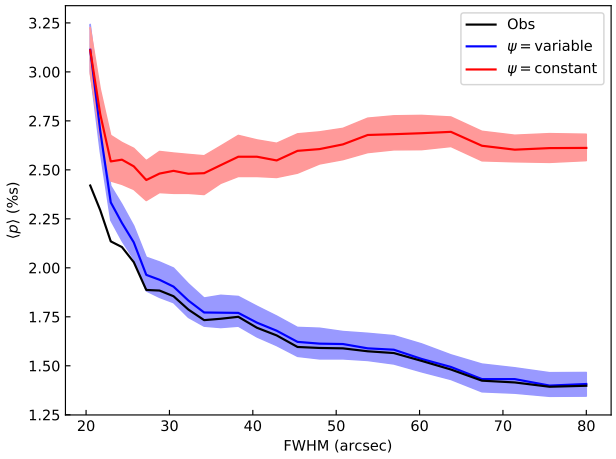

Fig. C.5. Simulation of $\langle p \rangle$ for POL-2 data with $N(H_2) > 10^{22}$ cm^{-2} as a function of the resolution. The black line shows the relation for the original observations. The blue line corresponds to a case where (Q, U) observed at $20''$ resolution are taken as a model of the true signal, before adding observational noise and convolving to a lower resolution. The red curve shows the result for data with identical p and I but with a globally constant polarisation angle. The shaded regions show the [10%, 90%] ranges for the random realisations.

because the fitted dynamical range and the number of data points decrease. The significance also decreases below $N(H_2) \sim 10^{22}$ cm^{-2} when data become dominated by noise. In between, the observed slope is much steeper than in the simulations. We note that it is not necessary for the $p_{\rm mas}$ estimates be completely unbiased, because the bias should be the same both for the real and the simulated observations. The significance of the result could be decreased only if the uncertainties of Q and U were underestimated, for example because of artefacts caused by the spatial filtering or the mapping procedure.

In Fig. C.2 the slope was observed to change systematically as a function of the data resolution. We carried out separate calculation to examine the potential contribution of geometrical depolarisation to this relation. Using data with $N(H_2) > 10^{22}$ cm^{-2}, we plot in Fig. C.5 the observed average polarisation fraction $\langle p_{\rm mas} \rangle$ as a function of the spatial resolution. This is compared to two simulations that start with the $20''$ resolution observations. First simulation assumes that these observations represent the true (noiseless) polarisation data. We produce synthetic observations by adding noise according to the POL-2 error estimates and plot again $\langle p_{\rm mas} \rangle$ as a function of the resolution. This is thus identical to the actual observations, except for the added noise. In the second simulation (Q, U) are first rotated so that polarisation angle is the same in each pixel. This means that the resolution only affects the noise level but there is no geometrical depolarisation.

Figure C.5 shows that without geometrical depolarisation the $\langle p \rangle$ does not decrease beyond $FWHM \sim 30''$, in agreement with S/N plotted in Fig. 9. On the contrary, there is minor increase towards lower resolutions. This is probably caused by the negative correlation between p and $N(H_2)$, which means that, for a given column density threshold, the average S/N of polarised intensity decreases as a function of the beam size. The simulation that included polarisation angle variations naturally converges towards the observed curve. The results indicate that between the $20''$ and $80''$ resolutions, more than half of the drop is caused by geometrical depolarisation and a smaller part by the reduced noise bias.

Appendix D: Alternative RT models for polarised emission

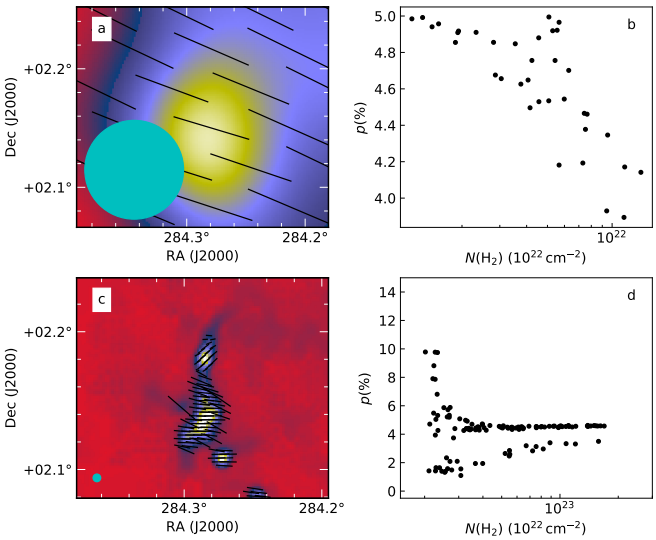

Fig. D.1. Predictions of polarised emission for a RT model with constant grain alignment, using the toy magnetic field model. The figure is the same as in Fig. 18 except that the transition from the large-scale field to different field orientations in the filament takes place at a higher threshold of $n(H_2) = 10^4$ cm^{-3}. The polarisation vectors are shown on the column density map in *panel a* and the p vs. $N(H_2)$ relation is plotted in *panel b* at *Planck* resolution. The lower panels are the corresponding plots for synthetic POL-2 observations.

In this section we show two variants of the polarisation models presented in Sect. 5.2.

Figure D.1 shows results for constant grain alignment. It is the same as Fig. 18 except that the transition from the uniform large-scale field to the filament field (as defined by the magnetic field toy model) takes place at a higher volume density threshold that is $n(H_2) = 10^4$ cm^{-3} instead of $n(H_2) = 3 \times 10^3$ cm^{-3}. This leads to decrease in the polarisation fractions, especially in the northern clump.

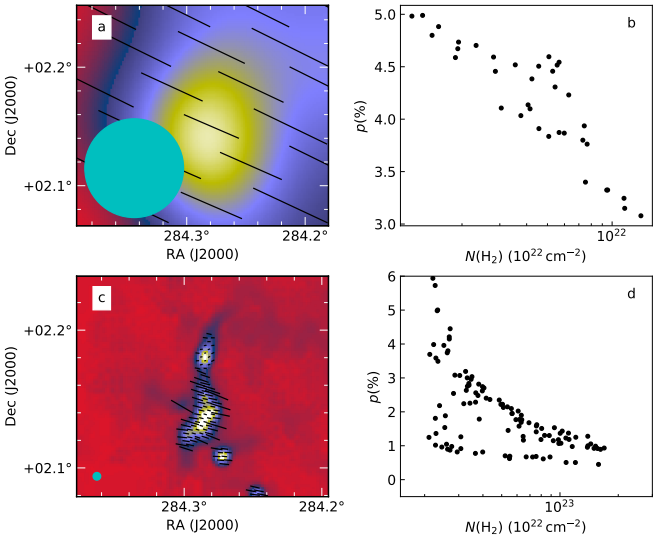

Fig. D.2. Model predictions for polarisation according to RAT grain alignment, assuming larger grain sizes. The figure is the same as Fig. 20 but the field orientation in the filament with $n(H_2) > 3 \times 10^3$ cm^{-3} is taken directly from POL-2 observations at 20″ resolution.

Figure D.2 corresponds to calculations with RAT grain alignment and grain sizes that are a factor of 2 larger than in the original dust model. The figure differs from Fig. D.2 in that the POS magnetic field orientations are taken from POL-2 observations instead of the toy model of Sect. 5.2. The polarisation fractions show a small decrease. Part of the changes may be caused by noise in the input polarisation angles, which here contributes to the geometrical depolarisation (that is, angle dispersion within the beam).